Multi-terminal transport measurements of MoS2 using a van der Waals heterostructure device platform

Multi-terminal transport measurements of MoS_2 using a van der Waals heterostructure device platform

Xu Cui[1‡], Gwan-Hyoung Lee[2‡*], Young Duck Kim[1‡], Ghidewon Arefe[1], Pinshane Y. Huang[3], Chul-Ho Lee[4], Daniel A. Chenet[1], Xian Zhang[1], Lei Wang[1], Fan Ye[5], Filippo Pizzocchero[6], Bjarke S. Jessen[6], Kenji Watanabe[7], Takashi Taniguchi[7], David A. Muller[3,8], Tony Low[9], Philip Kim[10], and James Hone[1*]

[1]Department of Mechanical Engineering, Columbia University, New York, NY 10027, USA

[2]Department of Materials Science and Engineering, Yonsei University, Seoul 120-749, Republic of Korea

[3]School of Applied and Engineering Physics, Cornell University, Ithaca, NY 14853, USA

[4]KU-KIST Graduate School of Converging Science and Technology, Korea University, Seoul 136-701, Republic of Korea

[5]Department of Material Science and Engineering, Columbia University, New York, NY 10027, USA

[6]DTU Nanotech, Technical University of Denmark, Ørsteds Plads, 345E, Kgs. Lyngby 2800, Denmark

[7]National Institute for Materials Science, 1-1 Namiki, Tsukuba 305-0044, Japan

[8]Kavli Institute at Cornell for Nanoscale Science, Ithaca, NY 14853, USA

[9]Department of Electrical & Computer Engineering, University of Minnesota, Minneapolis, MN 55455, USA

[10]Department of Physics, Harvard University, Cambridge, MA 02138, USA

‡These authors contributed equally.

Corresponding authors: gwanlee@yonsei.ac.kr and jh2228@columbia.edu

Atomically thin two-dimensional semiconductors such as MoS_2 hold great promise in electrical, optical, and mechanical devices and display novel physical phenomena. However, the electron mobility of mono- and few-layer MoS_2 has so far been substantially below theoretically predicted limits, which has hampered efforts to observe its intrinsic quantum transport behaviours. Potential sources of disorder and scattering include both defects such as sulfur vacancies in the MoS_2 itself, and extrinsic sources such as charged impurities and remote optical phonons from oxide dielectrics. To reduce extrinsic scattering, here we developed a van der Waals heterostructure device platform where MoS_2 layers are fully encapsulated within hexagonal boron nitride, and electrically contacted in a multi-terminal geometry using gate-tunable graphene electrodes. Magneto-transport measurements show dramatic improvements in performance, including a record-high Hall mobility reaching 34,000 cm^2/Vs for 6-layer MoS_2 at low temperature, confirming that low-temperature performance in previous studies was limited by extrinsic interfacial impurities rather than bulk defects in the MoS_2. We also observed Shubnikov-de Haas oscillations for the first time in high-mobility monolayer and few-layer MoS_2. Modeling of potential scattering sources and quantum lifetime analysis indicate that a combination of short-ranged and long-ranged interfacial scattering limits low-temperature mobility of MoS_2.

Following the many advances in basic science and applications of graphene, other two-dimensional (2D) materials, especially transition metal dichalcogenides (TMDCs), have attracted significant interest for their fascinating electrical, optical, and mechanical properties [1–8]. Among the TMDCs, semiconducting MoS_2 has been the mostly widely studied: it shows a thickness-dependent electronic band structure [3,5], reasonably high carrier mobility [1,2,6–9], and novel phenomena such as coupled spin-valley physics and the valley Hall effect [10–14], leading to various applications, such as transistors [1,7,15], memories [16], logic circuits [17,18], light-emitters [19], and photo-detectors [20] with flexibility and transparency [2,21]. However, as for any 2D material, the electrical and optical properties of MoS_2 are strongly affected by impurities and its dielectric environment [1,2,9,22], hindering the study of intrinsic physics and limiting the design of 2D-material-based devices. In particular, the theoretical upper bound of the electron mobility of monolayer (1L) MoS_2 is predicted to be from several tens to a few thousands at room temperature (T) and exceed 10^5 cm^2/Vs at low T depending on the dielectric environment, impurity density and charge carrier density [23–25]. In contrast, experimentally measured 1L MoS_2 devices on SiO_2 substrates have exhibited room-T two-terminal field-effect mobility that ranges from 0.1 - 55 cm^2/Vs [1,26,27]. This value increases to 15 - 60 cm^2/Vs with encapsulation by high-dielectric materials [1,9], owing to more effective screening of charged impurities [24]. Due to the presence of large contact resistance from the metal-MoS_2 Schottky barrier, however, these two-terminal measurements underestimate the true channel mobility [7,28,29]. Multi-terminal Hall mobility measurements [8,9] still show mobility substantially below theoretical limits, particularly at low T with best reported values of 174 cm^2/Vs at 4 K for 1L [9] and 250 cm^2/Vs and 375 cm^2/Vs at 5 K for 1L and 2L [8]. Typically, these thin samples exhibit a crossover to non-metallic behaviour at carrier densities below ~10^{13} cm^{-2} [8,9,30], or at smaller carrier densities by engineering

of local defect states and improving interfacial quality [31]. The scattering and disorder that leads to this non-metallic behaviour can arise from multiple origins such as lattice defects, charged impurities in the substrate and surface adsorbates, and it has been difficult to identify their separate contributions [1,8,9,23,30–33].

van der Waals heterostructure device platform

We have previously demonstrated that encapsulation of graphene within hBN reduces scattering from substrate phonons and charged impurities, resulting in band transport behaviour that is near the ideal acoustic phonon limit at room T, and ballistic over more than 15 μm at low T [34]. These results were realized with a novel technique to create one-dimensional edge contacts to graphene exposed by plasma-etching a hBN/graphene/hBN stack. Such an approach has not yet proved effective with MoS_2. However, recent reports that graphene can create a high quality electrical contact to MoS_2 [18,35] motivate a hybrid scheme, in which the channel MoS_2 and multiple graphene 'leads' are encapsulated in hBN, and the stack is etched to form graphene-metal edge contacts. This new scheme is distinct from previous approaches, in that the entire MoS_2 channel is fully encapsulated and protected by hBN, and that we achieve multi-terminal graphene contacts without any contamination from device fabrication process.

Figure 1a and 1b show a schematic diagram and optical micrograph of a Hall bar device structure. We employed a 'PDMS (Polydimethylsiloxane) transfer' technique [2] to place few-layer graphene flakes around the perimeter of an MoS_2 flake, encapsulate them between thicker hBN layers, and place the entire stack on a Si/SiO_2 wafer (Supplementary Fig. 1a). The stack was then shaped into Hall bar geometry such that hBN-encapsulated MoS_2 forms the channel. In the contact regions, graphene overlaps the MoS_2 and extends to the edge, where it is in turn

contacted by metal electrodes [34]. Details of the fabrication process are described in the Methods section and Supplementary Information S1. High-resolution scanning transmission electron microscopy (STEM) (Fig. 1c; see also Supplementary Fig. 1b for a larger clean interface area of > 3 μm) confirms that the stacking method can produce ultraclean interfaces free of residue that can be seen when an organic polymer film is used for stacking [36]. We note that while Ohmic contacts have also been achieved in metal-MoS_2 contacts by deposition of small work-function metals, vacuum annealing, and electrostatic gating[4, 17, 18], top-deposited metal electrodes are not compatible with hBN-encapsulation.

For this study, a series of samples with thickness from 1 - 6 layers (1L - 6L) was fabricated and measured. The number of layers was identified by Raman and photoluminescence (PL) (see Supplementary Information S2). All samples were obtained by mechanical exfoliation except for the 1L sample, for which we used chemical vapor deposition (CVD) grown monolayer MoS_2 because of the limited size of mechanically exfoliated monolayers. The CVD-grown MoS_2 single crystal has been shown to exhibit high quality from structural, electrical and optical measurements [37], although the process of transferring it from the growth substrate may introduce more contamination than for mechanically exfoliated flakes.

Gate-tunable graphene-MoS_2 contact

For each sample, we performed temperature-dependent two-probe measurements to examine the quality of the graphene contacts. Figure 2a shows output curves ($I_{ds} - V_{ds}$) of a 4L MoS_2 device at back-gate V_{bg} = 80 V. The response is linear at room T and remains linear to low T, indicating an Ohmic contact. Similar behaviour is seen for V_{bg} > 20 V, whereas gapped behaviour corresponding to non-Ohmic contact is seen for V_{bg} < 20 V. This is consistent with

previous studies which show a gate-tunable contact barrier between graphene and MoS_2 [18,35]. In addition, it establishes the gate voltage range over which multi-terminal measurements can be reliably performed. Figure 2b shows the measured four-terminal resistivity ρ (in log scale) of the same sample from V_{bg} = 20 V to 80 V (corresponding to carrier densities of ~ 4.8×10^{12} cm^{-2} to ~ 6.9×10^{12} cm^{-2}, respectively), and from room T to 12 K. ρ decreases with increasing V_{bg}, as expected for an n-type semiconductor. With decreasing temperature, ρ drops dramatically over the entire accessible range of V_{bg}, reaching 130 Ω at 12 K. All of the samples studied exhibited similar behaviour: n-type semiconducting behaviour and metallic temperature-dependence in the gate voltage accessible to four-terminal measurements.

By comparing the two- and four-terminal results, the contact resistance can be determined (see Supplementary Information S3). The results for the 4L MoS_2 device, as shown in Fig. 2c, directly demonstrate that the contact resistance can be tuned by back-gate voltage. In fact, a small contact resistance of ~ 2 kΩ·μm can be reliably achieved at large gate voltage at room T. This likely reflects primarily the graphene-MoS_2 junction resistance, since both the graphene resistance and the graphene-metal contact resistance should be substantially less [34]. Below V_{bg} = 20 V, the contact resistance increases upon cooling, indicating activated transport across a contact barrier. However, above V_{bg} = 20 V, the contact resistance decreases upon cooling, reaching a low-T value of ~ 1 kΩ·μm above V_{bg} = 50 V. This metallic behaviour directly demonstrates that low-resistance contacts, with no thermal activation, can be achieved at sufficiently high gate voltage. Similar behaviour was observed in all samples (Supplementary Fig. 3), with contact resistance at high V_{bg} ranging from ~ 2 - 20 kΩ·μm at room T and ~ 0.7 - 10 kΩ·μm at low T. These values are comparable to room-T values reported previously for graphene [38] and metal [39–41] contacts, but larger than the best contacts achieved by MoS_2 phase engineering

(0.2 - 0.3 kΩ·μm) [29] . Due to the increase in band gap with decreasing thickness, the value of V_{bg} required to achieve Ohmic contact is larger for thinner samples.

Scattering mechanism in MoS_2

To examine the quality of the hBN-encapsulated devices and determine the scattering mechanisms limiting the carrier mobility of MoS_2, the Hall mobility $\mu_{Hall}(T)$ was derived from $\rho(T)$ and the carrier density $n(V_{bg})$ (obtained by Hall effect measurements, see Supplementary Information S4). Figure 3a shows μ_{Hall} for the 1L - 6L samples as a function of temperature, at carrier densities varying from 4.0×10^{12} cm^{-2} to 1.2×10^{13} cm^{-2} (see Fig. 3b and Supplementary Table 1). Thinner samples were measured at higher carrier densities required to achieve Ohmic contacts. For all of the samples, mobility increases with decreasing temperature and saturates at a constant value at low *T*. The low-*T* mobility in our devices is much higher than previously reported values, and there is no sign of metal-insulator transition as observed at similar carrier densities around 10^{13} cm^{-2} in SiO_2-supported MoS_2 [8,9,30,32,33] . This strongly suggests that extrinsic scattering and disorder (either from SiO_2 or from processing with polymer resists) has been the primary source of non-metallic behaviour in MoS_2 measured to date.

The measured mobility curves can be reasonably fitted to a simple functional form: $\frac{1}{\mu(T)} = \frac{1}{\mu_{imp}} + \frac{1}{\mu_{ph}(T)}$, where μ_{imp} is the contribution from impurity scattering, and μ_{ph} is the temperature-dependent contribution due to phonon scattering. In all samples, the fitted $\mu_{ph}(T)$ is well described by a power law $\mu_{ph} \sim T^{-\gamma}$ above 100 K (Supplementary Fig. 7). This behaviour is consistent with mobility limited by MoS_2 optical phonons, as theoretically predicted to have an exponent of ~ 1.69 in monolayer [23] and ~ 2.5 for bulk MoS_2 [42] at T > 100 K. Although this power

law behaviour has been observed in experiments by other groups [8,9,30], a stronger temperature dependence was observed in our devices, with the exponent γ ranging from 1.9 - 2.5 (inset table of Fig. 3a), as opposed to 0.55 - 1.7 reported previously [8,9,30]. We also note that the room-*T* mobility, which is dominated by phonon scattering in all of the samples, is seen to vary from 40 - 120 cm^2/Vs. At this point we can find no satisfactory explanation for this variation: there is no discernible trend with thickness, and no variation of the gamma value with carrier density (see Supplementary Fig. 8). Finally, we note that a deviation from the simple form $\mu_{ph} \sim T^{-\gamma}$ in high mobility samples below 100 K may indicate acoustic phonon scattering, although further study is needed to fully explore this regime.

At the lowest temperature, phonon scattering is suppressed, and the residual resistivity is due to dominant long-ranged Coulomb impurities or short-ranged atomic defects [43–45], captured in the measured quantity μ_{imp}. Figure 3b shows the derived values of μ_{imp} as a function of carrier density *n*. For each sample, μ_{imp} increases with *n*, with maximum values ranging from 1,020 cm^2/Vs in the CVD monolayer to 34,000 cm^2/Vs for 6L, up to two orders of magnitude higher than previously reported values [8,46] (Fig. 3b and Supplementary Table 1). These basic trends allow us to rule out scattering due to impurities or defects located within the MoS_2 itself: bulk charged impurities should give rise to thickness-independent mobility, and short-ranged scatterers due to atomic defects should give rise to a density-independent mobility [45]. On the other hand, interfacial scatterers, including both Coulomb impurities and short-ranged defects, which are limiting scattering mechanisms in high quality conventional 2D electron gas system [44] are promising candidates. Indeed, PDMS transfer, while substantially cleaner than methods involving organic polymers, can potentially introduce adsorbates to the top MoS_2 surface.

To understand the effects of interfacial scattering on samples with different thickness, we model interfacial Coulomb and short-range scattering as a function of carrier density, for samples from 1L to 6L in thickness. For Coulomb scattering, we employed a model based on a perturbative approach by Stern [47], from which we obtained the screened Coulomb potential used in the mobility calculation. This model has also been commonly used in the context of semiconductor devices (see Supplementary Information S8). Within the model, increasing carrier density enhances screening of the interfacial Coulomb potential, which leads to improved carrier mobility, and increasing the thickness of MoS_2 redistributes the charge centroid further from the interface, also resulting in enhancement of mobility. The calculated mobility is shown in Fig. 3c, assuming the same impurities concentration of 6×10^9 cm^{-2} (chosen to match the 6L data) located at the top MoS_2 interface across devices with different number of layers. Although the qualitative trend of increasing mobility with layer numbers and carrier densities is consistent with the model, the model fails to account for the observed large thickness dependence of more than an order of magnitude between the 1L and 6L devices. The changes in the model calculations including the effects of band structure change with increasing layer thickness is discussed in Supplementary Information S8.

We next consider interfacial short-ranged scatterers with atomically localized scattering potentials, which can be modeled as delta-function potentials within the same framework as used above. Quantum lifetime measurements, to be discussed later, suggest that these scatterers strongly dominate electronic transport in the 1L devices. We therefore set the interfacial short-ranged scattering parameter (the product of scattering potential and defect density, see Supplementary Information S8) to fit the mobility of the 1L device. In this case, for the same

interfacial scattering the mobility increases rapidly with sample thickness – much more than observed experimentally.

Based on this analysis, we propose that the interfaces in our devices introduce both long-ranged Coulomb scattering and short-ranged scattering. In this case, we can calculate the total extrinsic mobility using Matthiessen's rule. The combination of long-ranged and short-ranged scatterers provides a better agreement to the observed layer-dependent mobility as shown in Fig. 3e, a salient point which we will revisit again later in quantum oscillations study. Of course, a perfect match to experiment is not expected due to sample-to-sample variation in impurity density. We also note that the long-ranged impurity density of 6×10^9 cm^{-2} is two orders of magnitude smaller than typically obtained for graphene on SiO_2, and hence accounts for the two orders of magnitude larger mobility we obtained as compared to the best reported devices [8,46] .

Observation of Shubnikov-de Haas (SdH) oscillations in MoS_2

Figure 4 shows the longitudinal (R_{xx}) and Hall resistance (R_{xy}) of the monolayer (Fig. 4a), 4L MoS_2 (Fig. 4b) and 6L MoS_2 (Fig. 4c) samples as a function of applied magnetic field. We observe pronounced SdH oscillations in MoS_2 for the first time, providing additional strong evidence of high quality and homogeneity in the heterostructure devices. In the highest-mobility (6L) sample (Fig. 4c), the onset of SdH oscillations is close to 1 Tesla (T), further confirming its ultra-high mobility. Encouragingly, the high-field Hall resistance (blue curve, R_{xy}) begins to reveal plateau-like structures at high magnetic fields coinciding with R_{xx} minima. These emerging features were similarly observed in early studies of graphene samples with moderate mobility [48] , giving hope that fully developed quantum Hall states can be observed with further improvements in sample quality. The periodicity of the SdH oscillations can be used to estimate

the carrier density, or equivalently to measure the level degeneracy g for a known density (for details see Supplementary S7). For the 1L samples, we observe $2 < g < 4$, indicating that the bands may be partially valley-spin split (the multi-band nature of the 6L sample complicates this analysis). This is consistent with extra SdH oscillations that begin to emerge at high fields, but more detailed study is required to explore this splitting in detail.

The quantum scattering time τ_q which is limited by both small and large angle scattering that destroys quantized cyclotron orbits, can be estimated from the magnetic field corresponding to the onset of SdH oscillations, following the relation $\mu_q = e\,\tau_q/m^* \sim 1/B_q$ [49], where e is the electron charge and m^* is the effective mass obtained from *ab initio* bandstructure calculations [50]. This yields quantum mobilities for 1L, 4L and 6L MoS_2 of ~ 1,400 cm^2/Vs, ~ 3,100 cm^2/Vs and ~ 10,000 cm^2/Vs, respectively. A more accurate estimate of τ_q in MoS_2 can be obtained using a Dingle plot (Supplementary Fig. 9), a well-established method in conventional 2D electron gas systems (2DEGs) (for details see Supplementary S6). The inset of Fig. 4a shows SdH oscillations of 1L MoS_2, after subtraction of a magnetoresistance background, as function of $1/B$. The red dashed line is the fitted envelope, from which we estimate a quantum scattering time of $\tau_q = 176$ fs. We show the values of τ_q obtained using both methods (oscillation onset and Dingle plots) in Supplementary Fig. 9c. The ratio of transport to quantum scattering time can provide additional evidence of predominant scattering sources. In our samples a ratio near 1 in 1L devices indicates predominantly short-ranged scattering, and an increase in τ_t/τ_q with increasing thickness indicates a crossover to long-range scattering. This trend consistent with our previous physical picture of low-T electronic transport dominated by a mix of short- and long-ranged interfacial impurities.

Conclusion

We demonstrate a vdW heterostructure device platform in which an atomically thin MoS_2 layer is encapsulated by hBN and contacted by graphene. The vdW heterostructure provides a standard device platform that enables us to measure intrinsic electrical transport of 2D materials and achieve high mobility 2D devices for studying the unique transport properties and novel quantum physics. By forming robust and tunable electrical contacts and dramatically reducing interfacial impurities, intrinsic electron-phonon scattering can be observed at high *T*, and substantially improved mobility can be achieved at low *T*. This enables the first observation of Shubnikov-de Haas oscillations in MoS_2. Modeling and quantum lifetime analysis suggest that a combination of short-ranged and long-ranged interfacial scattering limits the low-*T* mobility, indicating that further improvements should be possible.

Methods

Device fabrication. The hBN/MoS_2/graphene/hBN stacks were fabricated using the 'PDMS transfer' [2] technique on 285 nm SiO_2/Si substrates. The transfer techniques are described in detail in the Supplementary Information S1. The stacks were then shaped to the desired Hall bar structure through electron-beam patterning and reactive ion etching (RIE) with a mixture of CHF_3 and O_2. Finally, metal leads were patterned by e-beam lithography and subsequent deposition of metals (Cr 1nm/Pd 20nm/Au 50nm). The metal leads make edge-contact to graphene electrodes as reported previously [34].

TEM sample preparation. For high-resolution imaging, we fabricated a cross-sectional TEM lift-out sample from the finished encapsulated devices, using a FEI Strata 400 dual-beam Focused Ion Beam. STEM imaging was conducted in a FEI Tecnai F-20 STEM operated at

200kV, with a 9.6 mrad convergence semiangle and high-angle annular dark field detector. False coloring was added by hand.

Electrical measurements and magneto-transport measurements. Two-terminal transport characteristics were measured by applying DC bias (Keithley 2400) to the source and gate electrodes and measuring the drain current using a current amplifier (DL 1211). For four-terminal measurements, a standard lock-in amplifier (SR830) measured voltage drop across the channel with constant current bias. Magneto-transport measurements were performed in a Physical Property Measurement System (PPMS) (Fig. 4c) and a He_3 cryostat at the National High Magnetic Field Laboratory (NHMFL) (Fig. 4a and b).

References

1. Radisavljevic, B., Radenovic, A., Brivio, J., Giacometti, V. & Kis, A. Single-layer MoS_2 transistors. *Nature Nanotech.* **6**, 147–150 (2011).
2. Lee, GH. *et al.* Flexible and transparent MoS_2 field-effect transistors on hexagonal boron nitride-graphene heterostructures. *ACS Nano* **7**, 7931-7936 (2013).
3. Mak, K., Lee, C., Hone, J., Shan, J. & Heinz, T. Atomically Thin MoS_2: A New Direct-Gap Semiconductor. *Phy. Rev. Lett.* **105**, 136805 (2010).
4. Lee, C. H. *et al.* Atomically thin p–n junctions with van der Waals heterointerfaces. *Nature Nanotech.* **9**, 676-681 (2014).
5. Lee, C. *et al.* Anomalous lattice vibrations of single-and few-layer MoS_2. *ACS Nano* **4**, 2695-2700 (2010).
6. Kim, S. *et al.* High-mobility and low-power thin-film transistors based on multilayer MoS_2 crystals. *Nature Commun.* **3**, 1011 (2012).
7. Das, S., Chen, H.-Y., Penumatcha, A. & Appenzeller, J. High Performance Multilayer MoS_2 with Scandium Contacts. *Nano Lett.* **13**, 100-105 (2013).
8. Baugher, B., Churchill, H., Yang, Y. & Jarillo-Herrero, P. Intrinsic Electronic Transport Properties of High-Quality Monolayer and Bilayer MoS_2. *Nano Lett.* **13**, 4212–4216 (2013).
9. Radisavljevic, B. & Kis, A. Mobility engineering and a metal–insulator transition in monolayer MoS_2. *Nature Mater.* **12**, 815–820 (2013).
10. Xiao, D., Liu, G.-B., Feng, W., Xu, X. & Yao, W. Coupled Spin and Valley Physics in Monolayers of MoS_2 and Other Group-VI Dichalcogenides. *Phys. Rev. Lett* **108**, 196802 (2012).
11. Mak, K., McGill, K., Park, J. & McEuen, P. Valleytronics. The valley Hall effect in MoS_2 transistors. *Science* **344**, 1489–1492 (2014).

12. Zeng, H., Dai, J., Yao, W., Xiao, D. & Cui, X. Valley polarization in MoS_2 monolayers by optical pumping. *Nature Nanotech.* **7**, 490–493 (2012).
13. Jiang, T. *et al.* Valley and band structure engineering of folded MoS_2 bilayers. *Nature Nanotech.* **9**, 825-829 (2014).
14. Mak, K., He, K., Shan, J. & Heinz, T. Control of valley polarization in monolayer MoS_2 by optical helicity. *Nature Nanotech.* **7**, 494-498 (2012).
15. Bao, W., Cai, X., Kim, D., Sridhara, K. & Fuhrer, M. High mobility ambipolar MoS_2 field-effect transistors: Substrate and dielectric effects. *Applied Physics Letters* **102,** 042104 (2013).
16. Choi, M., Lee, GH., Yu, Y., Lee, D. & Lee, S. Controlled charge trapping by molybdenum disulphide and graphene in ultrathin heterostructured memory devices. *Nature Commun.* **4**, 1642 (2013).
17. Wang, H. *et al.* Integrated circuits based on bilayer MoS_2 transistors. *Nano Lett.* **12**, 4674-4680 (2012).
18. Yu, L. *et al.* Graphene/MoS_2 Hybrid Technology for Large-Scale Two-Dimensional Electronics. *Nano Lett.* **14**, 3055–3063 (2014).
19. Sundaram, R., Engel, M., Lombardo, A. & Krupke, R. Electroluminescence in single layer MoS_2. *Nano Lett.* **13**, 1416-1421 (2013).
20. Britnell, L. *et al.* Strong Light-Matter Interactions in Heterostructures of Atomically Thin Films. *Science* **340,** 1311–1314 (2013).
21. Yoon, J. *et al.* Highly Flexible and Transparent Multilayer MoS_2 Transistors with Graphene Electrodes. *Small* **9**, 3295-3300 (2013).
22. Qiu, H. *et al.* Electrical characterization of back-gated bi-layer MoS_2 field-effect transistors and the effect of ambient on their performances. *Appl. Rhys. Lett.* **100**, 123104 (2012).
23. Kaasbjerg, K., Thygesen, K. & Jacobsen, K. Phonon-limited mobility in n-type single-layer MoS_2 from first principles. *Phy. Rev. B* **85**, 115317 (2012).
24. Ma, N. & Jena, D. Charge Scattering and Mobility in Atomically Thin Semiconductors. *Phys. Rev. X* **4**, 011043 (2014).
25. Li, X. *et al.* Intrinsic electrical transport properties of monolayer silicene and MoS_2 from first principles. *Phys. Rev. B* **87**, 115418 (2013).
26. Novoselov, K. *et al.* Two-dimensional atomic crystals. *Proceedings of the National Academy of Sciences of the United States of America* **102,** 10451–10453 (2005).
27. Kappera, R, Voiry, D, Yalcin, SE, Jen, W & Acerce, M. Metallic 1T phase source/drain electrodes for field effect transistors from chemical vapor deposited MoS_2. *Appl. Rhys. Lett.* **2**, 092516 (2014).
28. Guo, Y. *et al.* Study on the Resistance Distribution at the Contact between Molybdenum Disulfide and Metals. *ACS Nano* **8**, 7771-7779 (2014).
29. Kappera, R. *et al.* Phase-engineered low-resistance contacts for ultrathin MoS_2 transistors. *Nature Mater.* **13**, 1128-1134 (2014).
30. Schmidt, H. *et al.* Transport Properties of Monolayer MoS_2 Grown by Chemical Vapor Deposition. *Nano Letters* **14,** 1909–1913 (2014).
31. Yu, Z. *et al.* Towards intrinsic charge transport in monolayer molybdenum disulfide by defect and interface engineering. *Nature Commun.* **5**, 5290 (2014).
32. Zhu, W. *et al.* Electronic transport and device prospects of monolayer molybdenum disulphide grown by chemical vapour deposition. *Nature Commun.* **5**, 3078 (2014).
33. Qiu, H. *et al.* Hopping transport through defect-induced localized states in molybdenum

disulphide. *Nature Commun.* **4**, 2642 (2013)
34. Wang, L. *et al.* One-Dimensional Electrical Contact to a Two-Dimensional Material. *Science* **342,** 614–617 (2013).
35. Roy, T. *et al.* Field-Effect Transistors Built from All Two-Dimensional Material Components. *ACS Nano* **8**, 6256-6264 (2014).
36. Haigh, S., Gholinia, A., Jalil, R., Romani, S. & Britnell, L. Cross-sectional imaging of individual layers and buried interfaces of graphene-based heterostructures and superlattices. *Nature Mater.* **11**, 764-767 (2012).
37. Zande, AM van der *et al.* Grains and grain boundaries in highly crystalline monolayer molybdenum disulphide. *Nature Mater.* **12**, 554-561 (2013).
38. Du, Y., Yang, L., Liu, H. & Ye, P. Contact research strategy for emerging molybdenum disulfide and other two-dimensional field-effect transistors. *APL Materials* **2,** 092510 (2014).
39. Das, S. & Appenzeller, J. Where does the current flow in two-dimensional layered systems? *Nano Lett.* **13,** 3396–3402 (2013).
40. Liu, H., Neal, A. T. & Ye, P. D. Channel length scaling of MoS_2 MOSFETs. *ACS Nano* **6**, 8563–8569 (2012).
41. Liu, H. *et al.* Switching Mechanism in Single-Layer Molybdenum Disulfide Transistors: An Insight into Current Flow across Schottky Barriers. *ACS Nano* **8**, 1031–1038 (2013).
42. Fivaz, R. & Mooser, E. Mobility of Charge Carriers in Semiconducting Layer Structures. *Phys. Rev.* **163**, 743755 (1967).
43. Chen, J.-H., Jang, C., Xiao, S., Ishigami, M. & Fuhrer, M. S. Intrinsic and extrinsic performance limits of graphene devices on SiO_2. *Nature Nanotech.* **3,** 206–209 (2008).
44. Ando, T., Fowler, A. B. & Stern, F. Electronic properties of two-dimensional systems. *Rev. Mod. Phys.* **54,** 437 (1982).
45. Sarma, D., Adam, S., Hwang, E. & Rossi, E. Electronic transport in two-dimensional graphene. *Rev. Mod. Phys.* **83,** 407 (2011).
46. Neal, A., Liu, H., Gu, J. & Ye, P. Magneto-transport in MoS_2: phase coherence, spin-orbit scattering, and the hall factor. *ACS Nano* **7**, 7077–1082 (2013).
47. Stern, F. & Howad W. E. Properties of Semiconductor Surface Inversion Layers in the Electric Quantum Limit. Phys. Rev.**163**, 816. (1967)
48. Novoselov, K. *et al.* Electric Field Effect in Atomically Thin Carbon Films. *Science* **306,** 666–669 (2004).
49. Kretinin, A. V. *et al.* Electronic properties of graphene encapsulated with different two-dimensional atomic crystals. *Nano Lett.* **14**, 3270–3276 (2014).
50. Liu, G.-B., Shan, W.-Y., Yao, Y., Yao, W. & Xiao, D. Three-band tight-binding model for monolayers of group-VIB transition metal dichalcogenides. *Physical Review B* **88,** 085433 (2013).

Acknowledgements

This research was supported by the U.S. National Science Foundation (DMR-1122594), the NSF MRSEC program through Columbia in the Center for Precision Assembly of Superstratic and Superatomic Solids (DMR-1420634), and in part by the FAME Center, one of six centers of STARnet, a Semiconductor Research Corporation program sponsored by MARCO and DARPA. G.H.L was supported by Basic Science Research Program (NRF-2014R1A1A1004632) through the National Research Foundation (NRF) funded by the Korean government Ministry of Science, ICT and Future Planning, and in part by the Yonsei University Future-leading Research Initiative of 2014. P.Y.H. acknowledges support from the NSF Graduate Research Fellowship Program under grant DGE-0707428. Additional support was provide through funding and shared facilities from the Cornell Center for Materials Research NSF MRSEC program (DMR-1120296). F.P. and B.S.J. acknowledged the Center for Nanostructured Graphene (CNG), which is funded by the Danish National Research Foundation, Project DNRF58. K.W. and T.T. acknowledge support from the Elemental Strategy Initiative conducted by the MEXT, Japan. T.T. acknowledges support a Grant-in-Aid for Scientific Research on Grant 262480621 and on Innovative Areas "NanoInformatics" (Grant 25106006) from JSPS. The high magnetic field measurements were performed at the NHMFL and the authors thank Alexey Suslov, Bobby Joe Pullum, Jonathan Billings, and Tim Murphy for assistance with the experiments at NHMFL.

Author Contributions

X.C. and G.H.L. designed the research project and supervised the experiment. X.C., G.H.L., Y.D.K., G.A., C.H.L., F.Y., F.P., B.S.J., and L.W. performed device fabrication and X.C.,

G.H.L. and Y.D.K. performed device measurements under supervision of P.K. and J.H.. X.C., G.H.L., G.A., X.Z. performed optical spectroscopy and data analysis. D.A.C. grew and prepared the CVD MoS_2 sample. T.L. performed the theoretical calculations. K.W. and T.T. prepared hBN samples. P.Y.H. and D.A.M. performed TEM analyses. X.C., G.H.L., Y.D.K. and J.H. analyzed the data and wrote the paper.

Figure Captions

Figure 1 | vdW device structure and interface characterization. a, Schematic of the hBN-encapsulated MoS_2 multi-terminal device. Exploded view shows the individual components that constitute the heterostructure stack. The bottom panel shows the zoom-in cross-sectional schematic of metal-graphene-MoS_2 contact region. **b,** Optical microscope image of a fabricated device. Graphene contact regions are outlined by dashed lines. **c,** Cross-section STEM image of the fabricated device. The zoom-in false-color image clearly shows the ultra-sharp interfaces between different layers. (graphene: 5L, MoS_2: 3L, top-hBN: 8 nm, bottom-hBN: 19 nm)

Figure 2 | Gate-tunable and temperature-dependent graphene-MoS_2 contact. a, Output curves (I_{ds} - V_{ds}) of the hBN-encapsulated 4L MoS_2 device with graphene electrodes at varying temperature. The back gate voltage (V_{bg}) is kept at 80 V with carrier density of 6.85×10^{12} cm^{-2} in MoS_2. The linearity of output curves confirms that graphene-MoS_2 contact is Ohmic at all temperatures. **b,** Resistivity (ρ) of 4L MoS_2 (log scale) as a function of V_{bg} at varying temperature. The resistivity decreases upon cooling, showing metallic behaviour, reaching ~ 130 Ω at 12 K. **c,** Contact resistance (R_C) of the same device (log scale) as a function of V_{bg} at varying temperature. The inset shows the R_C as a function of temperature at different V_{bg}. At high V_{bg}, contact resistance even decreases when decreasing the temperature.

Figure 3 | Temperature, carrier density dependence of Hall mobility and scattering mechanism. a, Hall mobility of hBN-encapsulated MoS_2 devices with different number of layers of MoS_2 as a function of temperature. To maintain Ohmic contacts, a finite V_{bg} was applied. The measured carrier densities from Hall measurements for each device are listed in Supplementary Table 1. The solid fitting lines are drawn by the model in the main text. All the fitting parameters are listed in Supplementary Table 1. For a visual guideline, a dashed line of power law $\mu_{ph} \sim T^{-\gamma}$ is drawn and fitted values of γ for each device are listed in the inset table. **b,** Impurity-limited mobility (μ_{imp}) as a function of carrier density of MoS_2. For comparison, the previously reported values from MoS_2 on SiO_2 substrates (Ref. 8, 46) are plotted. **c** to **e,** The solid lines show the theoretically calculated long-ranged (LR) impurity limited mobility (c), short-ranged (SR) impurity limited mobility (d) and mobility including both LR and SR based on Matthiessen's rule $1/\mu = 1/\mu_{LR}+1/\mu_{SR}$ as a function of carrier density for 1L to 6L MoS_2 (e). The experimental data from 1L and 6L are shown in dots (c-e).

Figure 4 | Observation of Shubnikov-de Haas oscillations in hBN-encapsulated MoS_2 device. **a,** Longitudinal resistance R_{xx} (red curve) and Hall resistance R_{xy} (blue curve) of hBN-encapsulated CVD 1L MoS_2 device as a function of magnetic field (B) measured at 0.3 K and carrier density of 9.7×10^{12} cm^{-2}. The inset shows the oscillation amplitude (black curve) as a function of 1/B after subtraction of the magneto-resistance background. The quantum scattering time extracted from the fitted Dingle plot (red dashed line) is 176 fs. **b,** R_{xx} (red curve) and R_{xy} (blue curve) of hBN-encapsulated 4L MoS_2 device as a function of B. Hall measurement was conducted at 0.3 K and carrier density of 4.9×10^{12} cm^{-2}. **c,** R_{xx} (red curve) and R_{xy} (blue curve) of hBN-encapsulated 6L MoS_2 device as a function of B. Hall measurement was conducted at 3 K and carrier density of 5.3×10^{12} cm^{-2}.

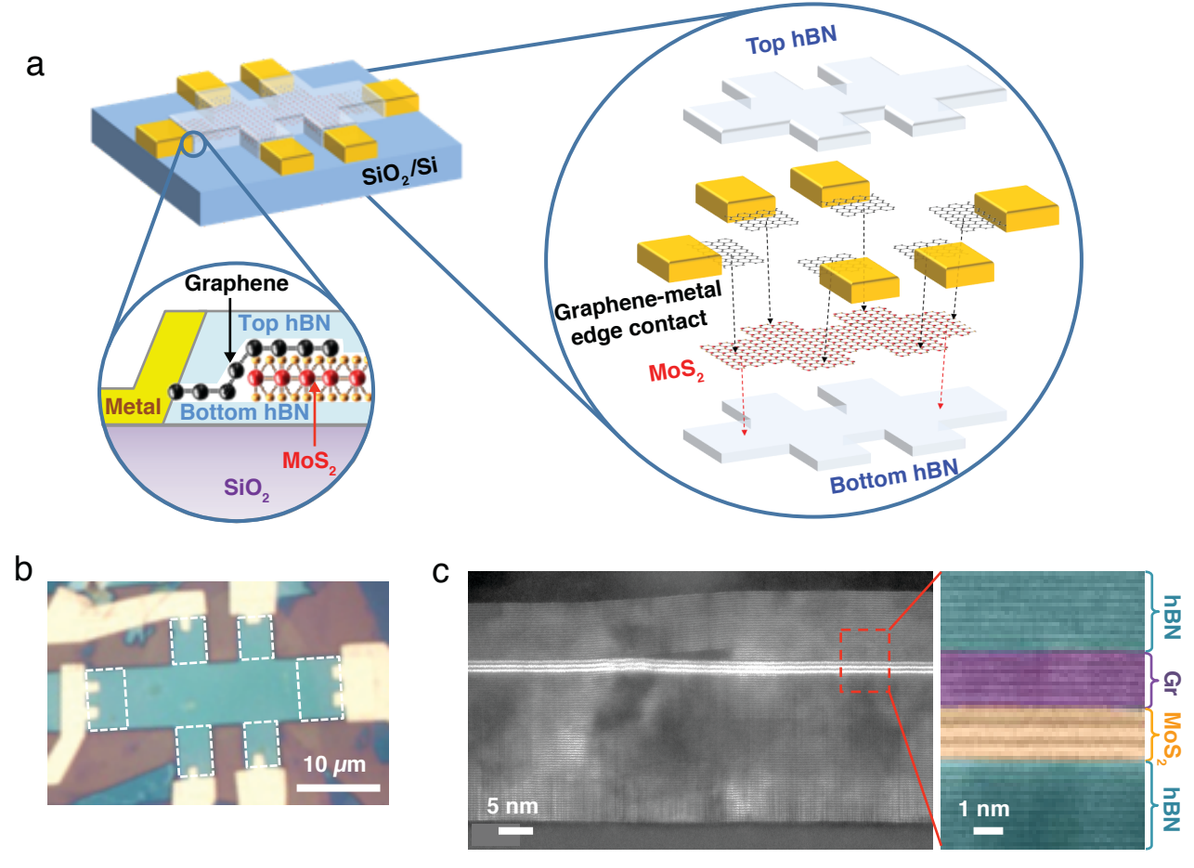
a
SiO2/Si
Graphene
Top hBN
Metal
Bottom hBN
MoS2
SiO2
Top hBN
Graphene-metal
edge contact
MoS2
Bottom hBN

b
10 μm

c
5 nm
1 nm
hBN
Gr
MoS2
hBN

a

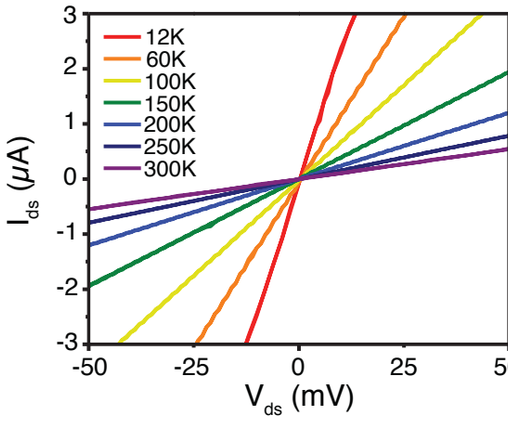
12K
60K
100K
150K
200K
250K
300K
I_ds (μA)
V_ds (mV)

b

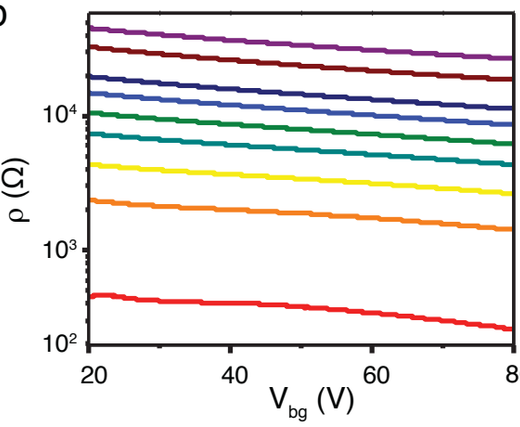
ρ (Ω)
V_bg (V)

c

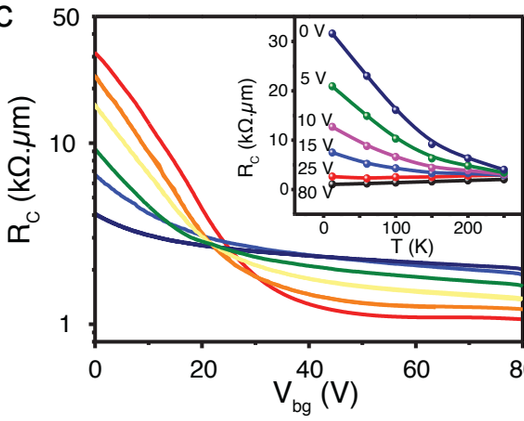
R_C (kΩ.μm)
V_bg (V)
0 V
5 V
10 V
15 V
25 V
80 V
T (K)

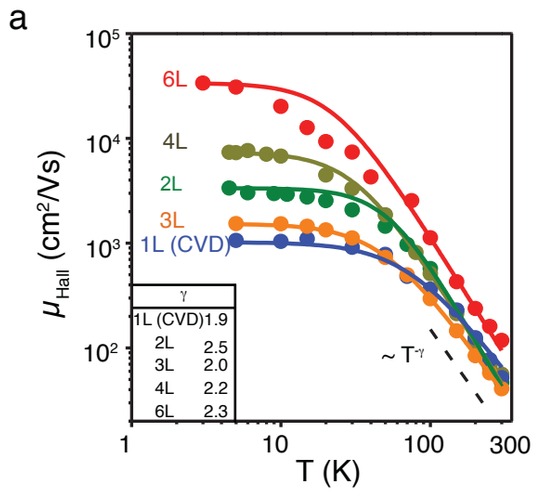
a
μ_{Hall} (cm²/Vs)
T (K)
6L
4L
2L
3L
1L (CVD)
γ
1L (CVD) 1.9
2L 2.5
3L 2.0
4L 2.2
6L 2.3
~ T^-γ

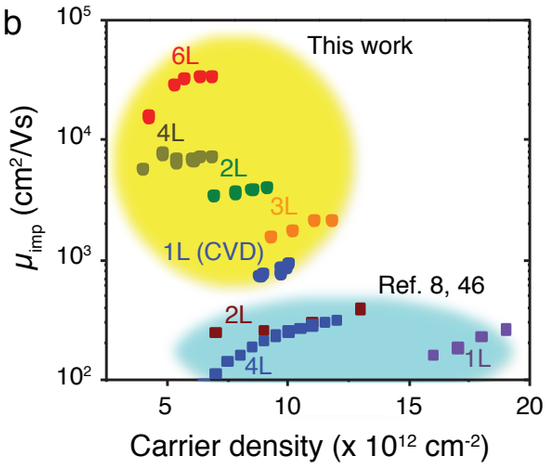
b
μ_{imp} (cm²/Vs)
Carrier density (x 10¹² cm⁻²)
This work
6L
4L
2L
3L
1L (CVD)
Ref. 8, 46
2L
4L
1L

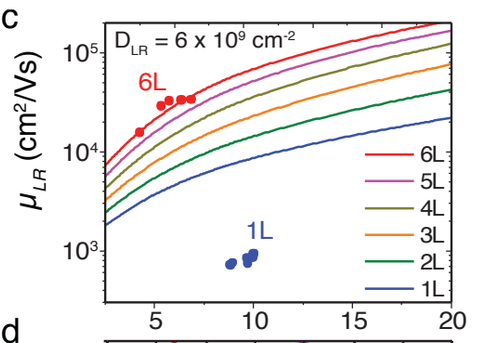
c
μ_{LR} (cm²/Vs)
D_{LR} = 6 x 10⁹ cm⁻²
6L
1L
6L
5L
4L
3L
2L
1L

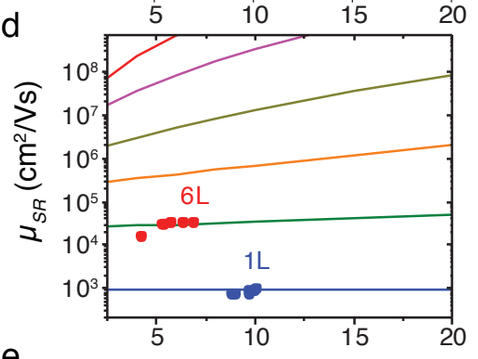
d
μ_{SR} (cm²/Vs)
6L
1L

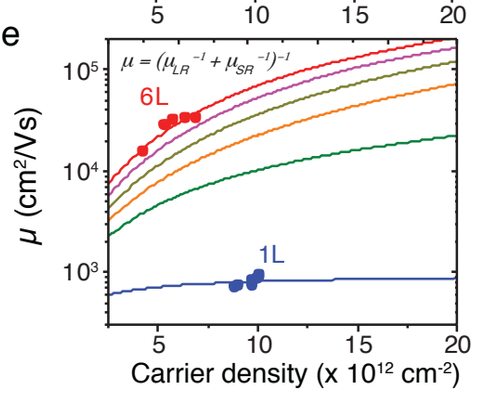
e
μ (cm²/Vs)
$\mu = (\mu_{LR}^{-1} + \mu_{SR}^{-1})^{-1}$
6L
1L
Carrier density (x 10¹² cm⁻²)

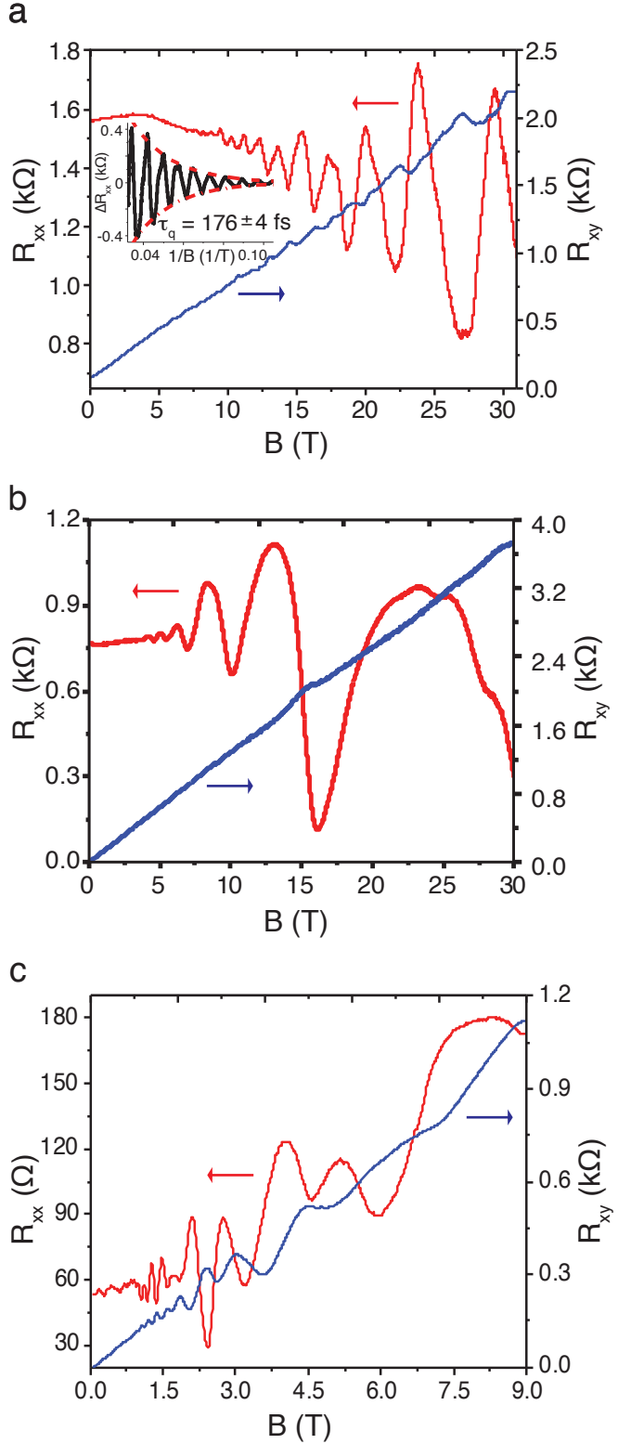
a
1.8
1.6
1.4
1.2
1.0
0.8
R_xx (kΩ)
2.5
2.0
1.5
1.0
0.5
0.0
R_xy (kΩ)
0
5
10
15
20
25
30
B (T)
0.4
0
-0.4
ΔR_xx (kΩ)
τ_q = 176 ± 4 fs
0.04
1/B (1/T)
0.10
b
1.2
0.9
0.6
0.3
0.0
R_xx (kΩ)
4.0
3.2
2.4
1.6
0.8
0.0
R_xy (kΩ)
0
5
10
15
20
25
30
B (T)
c
180
150
120
90
60
30
R_xx (Ω)
1.2
0.9
0.6
0.3
0.0
R_xy (kΩ)
0.0
1.5
3.0
4.5
6.0
7.5
9.0
B (T)

Supplementary Information for

Multi-terminal transport measurements of MoS_2 using a van der Waals heterostructure device platform

Xu Cui, Gwan-Hyoung Lee, Young Duck Kim, Ghidewon Arefe, Pinshane Y. Huang, Chul-Ho Lee, Daniel A. Chenet, Xian Zhang, Lei Wang, Fan Ye, Filippo Pizzocchero, Bjarke S. Jessen, Kenji Watanabe, Takashi Taniguchi, David A. Muller, Tony Low, Philip Kim, and James Hone

S1. Fabrication of hBN-encapsulated MoS_2 devices

As explained in our previous report[1], we directly exfoliated hexagonal boron nitride (hBN), MoS_2, and graphene flakes onto Polydimethylsiloxane (PDMS) stamps using mechanical exfoliation with Scotch tape and conducted multiple transfers onto hBN on a SiO_2 substrate. First, hBN flakes with a thickness of 10 - 30 nm were mechanically exfoliated onto 285nm SiO_2/Si chips. Then, MoS_2 (SPI Supplies) and few-layer graphene (Covalent Materials Co.) were separately prepared on PDMS stamps. The MoS_2 flake on the PDMS stamp was inverted and aligned onto the target hBN flake on the SiO_2 substrate by micro-manipulator and held in contact for 5 minutes at 40 °C in order to transfer the flake to the substrate. Next, graphene from PDMS was transferred to the hBN/MoS_2 stack and positioned to serve as electrodes. This step was repeated multiple times to place graphene electrodes around the perimeter of the MoS_2 channel. Finally, another hBN flake on PDMS was transferred on top of the hBN/MoS_2/graphene stack to provide complete encapsulation of the MoS_2 channel. The hBN/graphene/MoS_2/hBN stack was formed sequentially as shown in Fig. S1a (i-vii). We used e-beam lithography to shape the stack of hBN/graphene/MoS_2/hBN into a Hall bar geometry using patterned Poly(methyl methacrylate) (PMMA) as an etch mask as shown in Fig. S1a (viii). We performed a dry etching process using inductively coupled plasma (ICP, Oxford 80) with a mixture of CHF_3 and O_2 gas. The stack was etched until the edges of the graphene flakes were exposed (Fig. S1a (ix)). After dissolving the PMMA film in acetone, a second e-beam patterning was followed to define the metal leads. Metal leads of Cr (1 nm)/Pd (20 nm)/Au (50nm) was deposited by e-beam evaporation as shown in Fig. S1a(x). Ohmic contact is formed along edges of graphene between metal and graphene[2]. A cross-section STEM image in Fig. S1b confirms that the multi-stacked heterostructure with clean heterointerfaces can be achieved by this method.

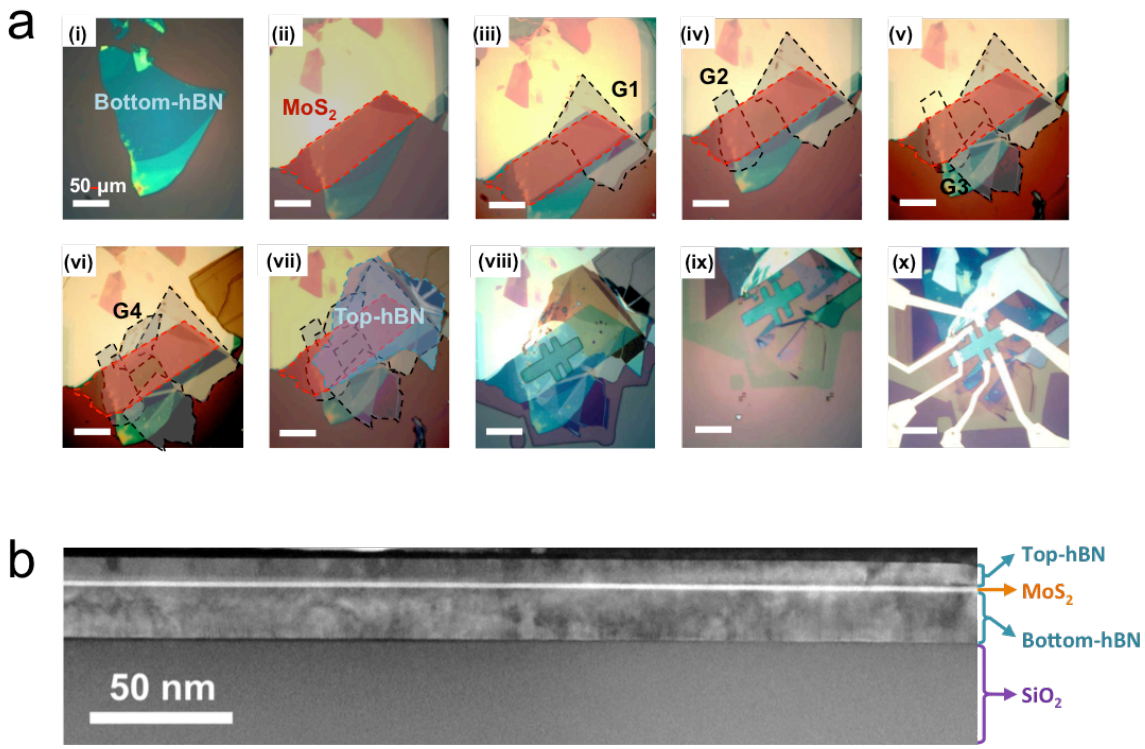

Supplementary Fig. 1 | Device fabrication process and ultra-clean heterointerfaces. a, Device fabrication process: (i) Bottom-hBN flake exfoliated onto a SiO_2/Si substrate. (ii) MoS_2 on hBN. MoS_2 was transferred onto bottom-hBN. (iii-vi) Four graphene flakes on hBN/MoS_2 stack. Four graphene flakes were sequentially transferred onto the stack around the perimeter of the MoS_2 channel. (vii) Top-hBN on graphene/MoS_2/hBN stack. Top-hBN was transferred on top of the stack for encapsulation. (viii) Patterning of PMMA into Hall bar geometry. PMMA layer in the stack was patterned by e-beam lithography into a Hall bar configuration. (ix) Dry etching of the stack. The stack is etched using PMMA as an etch mask. (x) Formation of metal leads. Metal leads are fabricated by e-beam lithography and deposition of metals. Scale bar: 50 μm. **b,** Cross-section STEM image of the stack (from top to bottom: hBN (8 nm), MoS_2 (3L), hBN (19 nm)). Scale bar: 50 nm.

S2. Identification of MoS_2 flakes on PDMS

We used Raman spectroscopy and photoluminescence (PL) measurements (in Via, Renishaw, 532 nm laser) to identify the number of layers of MoS_2 flakes on PDMS[3,4]. Figure S2a shows the PL spectra of a CVD-grown monolayer MoS_2. Bright-field optical images of few-layer MoS_2 exfoliated on PDMS are shown in Fig. S2b. The number of layers of these flakes was confirmed by the Raman spectra in Fig. S2c. We confirmed that MoS_2 flakes on PDMS have the correlation between Raman peak position difference of E^1_{2g} and A_{1g} modes and number of layers, which is consistent to our previous report[4].

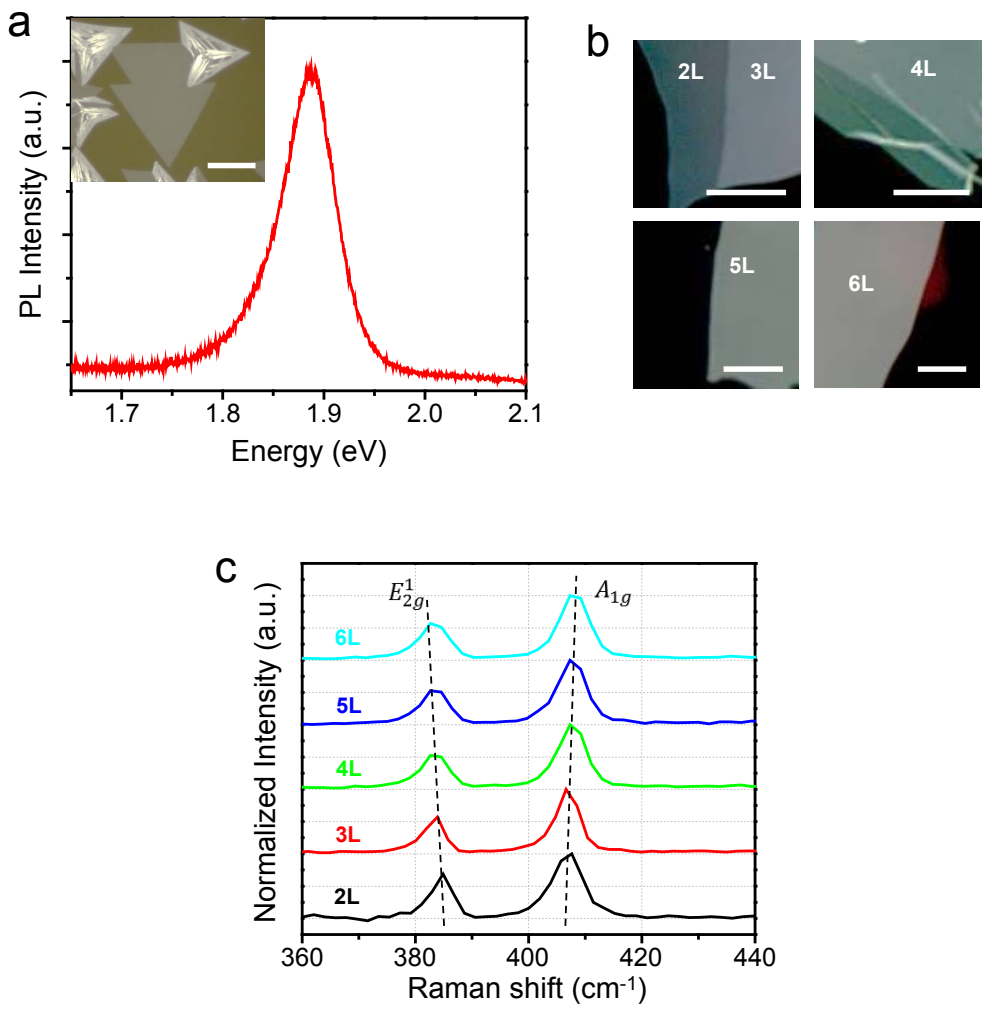

Supplementary Fig. 2 | Photoluminescence and Raman spectra of MoS_2 on PDMS a, PL spectra of CVD 1L MoS_2 on PDMS. The inset shows bright field optical image of CVD 1L MoS_2 on PDMS. **b,** Bright-field optical images of 2L to 6L MoS_2 flakes exfoliated on PDMS. Scale bar: 10 μm. **c,** Raman spectra of 2L to 6L MoS_2 on PDMS. As guided by the dashed lines, Raman peak position difference between E^1_{2g} and A_{1g} modes increases with MoS_2 thickness.

S3. Contact resistance and Schottky barrier of graphene-MoS_2 contacts

We estimate the contact resistance as $R_c = \frac{1}{2}(R_{2P} - R_{4P}\frac{L}{l})$, where R_{2P} is two-probe resistance, R_{4P} is the four-probe resistance of MoS_2, L is the two-probe length and l is four-probe length. The calculated contact resistance as a function of temperature and back gate voltage is shown in Fig. S3. Due to increase of the MoS_2 band gap with decreasing thickness from few-layers to monolayer[3], it is more difficult to form Ohmic contact, in other words lower Schottky barrier, for thinner MoS_2[1]. In this regard, graphene has been proved to be one of potential candidates as electrode for MoS_2[5,6]. A large gate-tunability of Fermi energy of graphene enables us to move graphene's Fermi level close to conduction band of MoS_2 by increasing back-gate voltage, resulting in reliable and stable Ohmic contact even for monolayer MoS_2 as shown in Fig. S3a. At reasonably high charge carrier concentration, contact resistance from ~ 0.7 k$\Omega\cdot\mu$m to 10 k$\Omega\cdot\mu$m can be reliably achieved across all samples at low temperature.

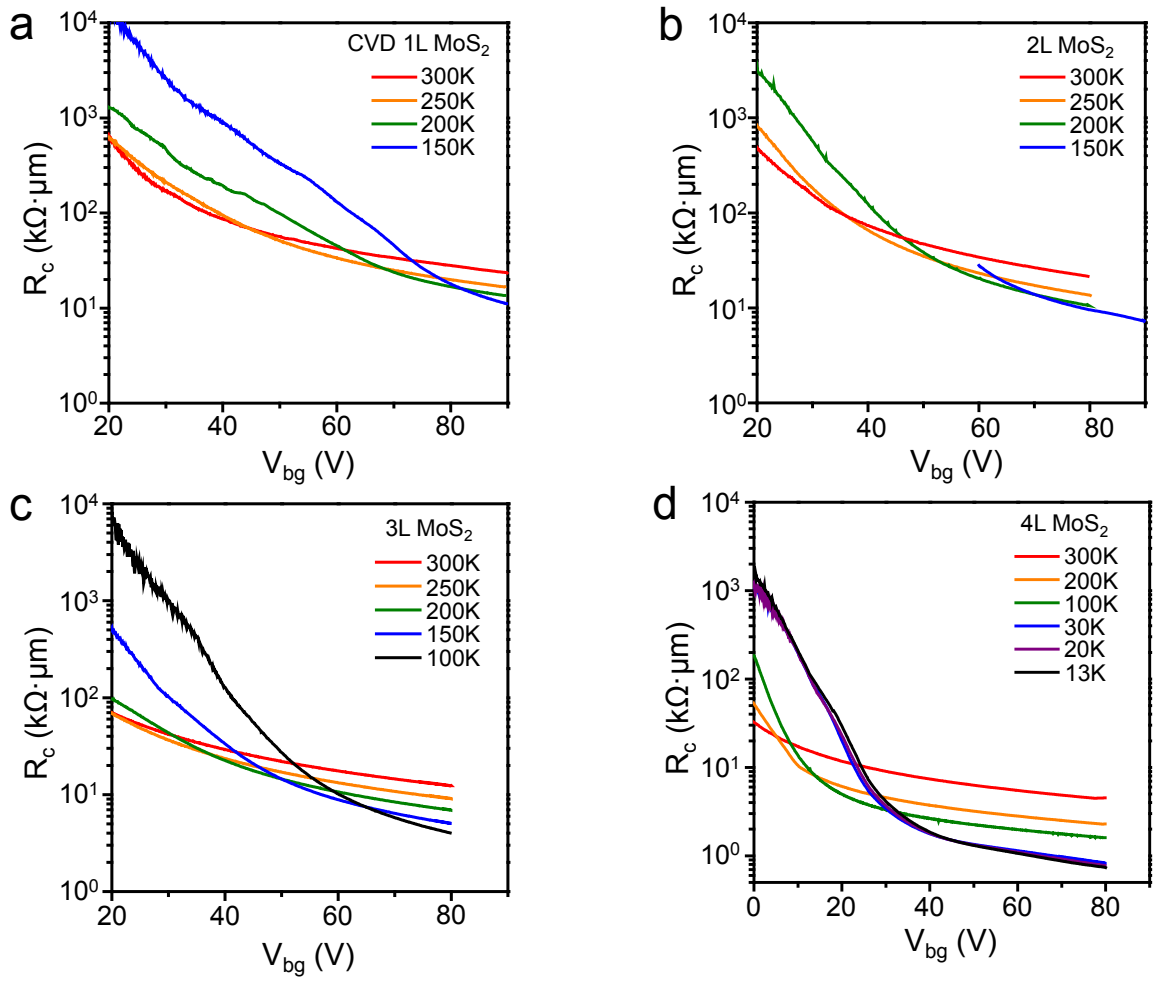

Supplementary Fig. 3 | Gate-tunable contact resistance of graphene-MoS_2 contact. Contact resistance as a function of back-gate voltage (V_{bg}) and temperature for 1L (CVD), 2L, 3L and 4L.

Furthermore, we calculated the Schottky barrier height of graphene-MoS_2 contact using the 2D thermionic emission relation[5],

$$I_d = AT^{3/2} \exp\left(\frac{-q\phi_B}{k_B T}\right) \left[\exp\left(\frac{qV_{\mathrm{ds}}}{\eta k_B T}\right) - 1\right],$$

where I_d, A, T, k_B, q, ϕ_B, and V_{ds} are drain current, the effective Richardson constant, temperature, the Boltzmann constant, electronic charge, the Schottky barrier height, and source-drain bias (50 mV), respectively. Here, η is an ideality factor, which is related with tunneling

effect contribution under high charge carrier concentration and at low temperature. To estimate the Schottky barrier height of graphene-MoS_2 with different back gate voltage (V_{bg}), we employed the Arrhenius plot, $\ln(I_d/T^{3/2})$ as a function of $1/k_BT$ as shown in Fig. S4. Because the slope of Arrhenius plot is the $-q\phi_B + qV_{ds}/\eta$, we can extract the Schottky barrier heights for different MoS_2 thickness. Here, we assume the ideality factor as $2 < \eta < 20$, and we check the availability of ideality factor from the Ohmic behavior in 2 probe output curve at low temperature. Fig. S5 exhibits the calculated Schottky barrier heights in hBN-encapsulated MoS_2 devices with different MoS_2 thickness. Large modulation of graphene's Fermi energy allows for the high tunability of the Schottky barrier height in graphene-MoS_2 contact, resulting in the small Schottky barrier height with relatively high V_{bg}. The Schottky barrier height becomes close to zero at V_{bg} of ~ 80V even for monolayer MoS_2, which enable us to form the Ohmic contact at very low temperature.

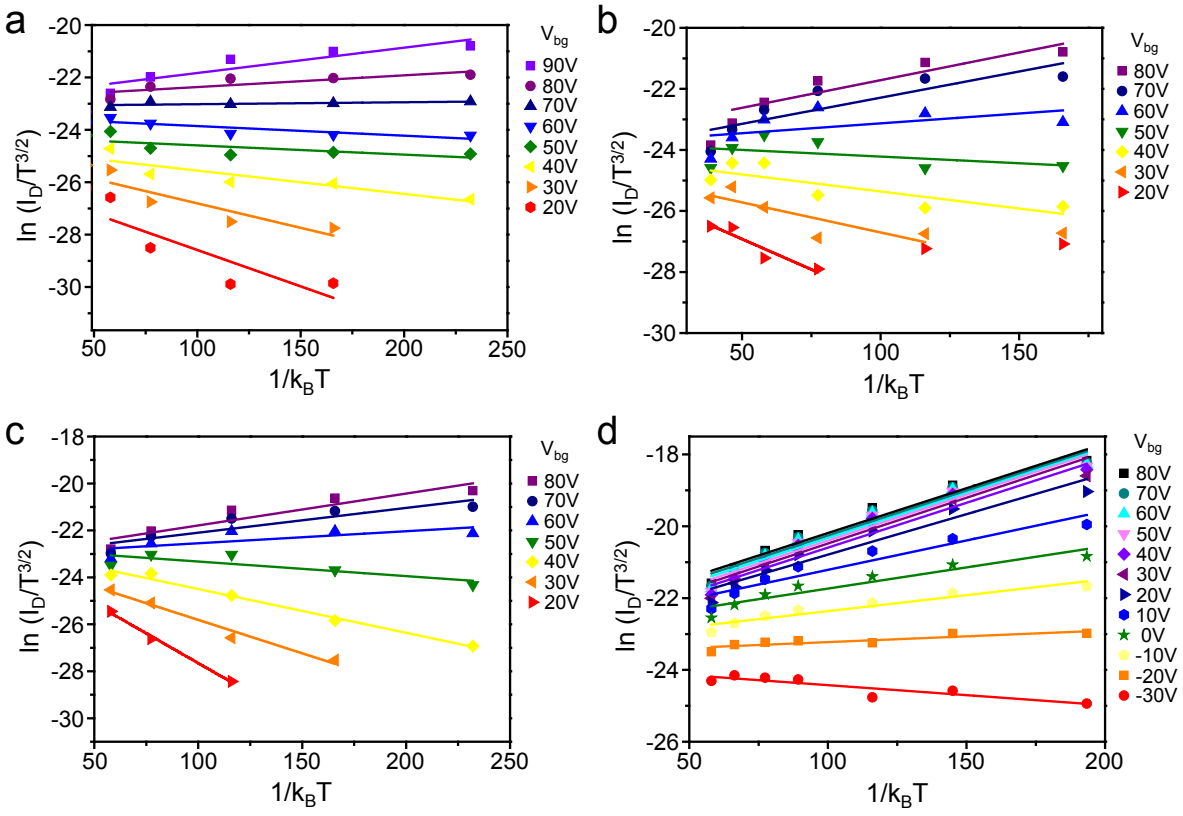

Supplementary Fig. 4 | Arrhenius plots of hBN-encapsulated MoS_2 devices for calculations of the Schottky barrier heights. a, 1L (CVD) **b,** 2L **c**, 3L **d,** 4L MoS_2.

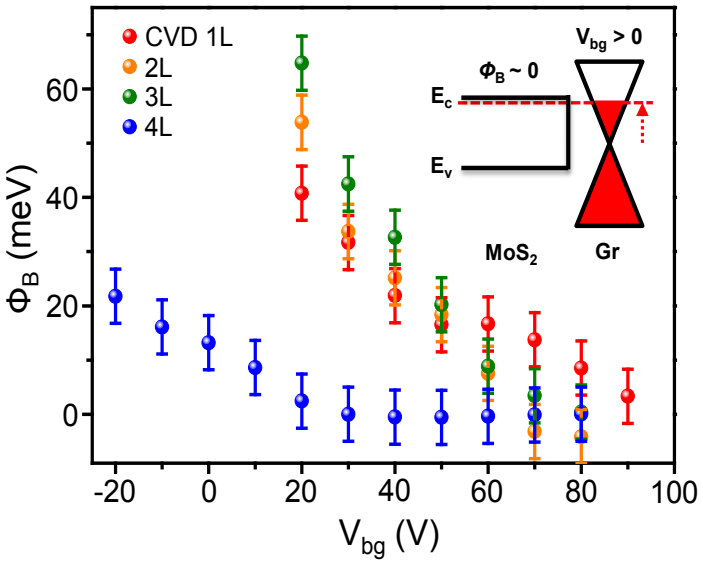

Supplementary Fig. 5 | Gate-voltage-tunability of the Schottky barrier heights in graphene-MoS_2 contacts. At higher back gate voltage, the Schottky barrier height can be reduced by modulation of graphene's Fermi level. The absence of Schottky barrier height enable us to form the Ohmic contact even at very low temperature.

S4. Hall measurements and Hall mobility calculations

In an hBN-encapsulated MoS_2 device, the Hall voltage and Hall mobility was measured with standard lock-in technique. In Fig. S6a, the Hall resistance (R_{xy}) was plotted as a function of magnetic field (B) at different V_{bg}. The total charge carrier concentration of MoS_2 (n) is obtained from $n_{Hall} = \frac{1}{e}\left(\frac{dB}{dR_{xy}}\right)$, where e and $\left(\frac{dB}{dR_{xy}}\right)$ are electron charge and magnetic-field-dependence of Hall resistance. As shown in Fig. S6a, R_{xy} is linearly dependent on the magnetic field at 10K and the calculated total charge carrier concentration has a linear relationship with applied back gate voltage (V_{bg}) as shown in Fig. S6b. These results confirm the validity of our Hall measurement at low temperature. With total charge carrier concentration, we estimate the Hall mobility from $\mu_{Hall} = \sigma/ne$, where μ_{Hall} is Hall mobility, σ is conductivity, n is total charge carrier concentration of MoS_2 and e is the electron charge.

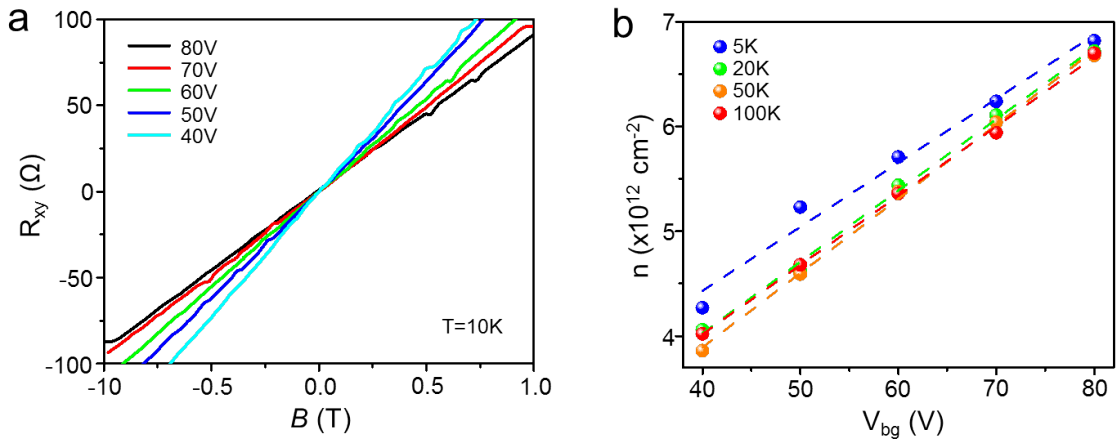

Supplementary Fig. 6 | Hall measurement and charge carrier concentration of MoS_2. a, Hall resistance (R_{xy}) at 10 K as a function of magnetic field (B) at different back gate voltage (V_{bg}) for 6L MoS_2. **b,** Charge carrier concentration of MoS_2 (n) calculated from Hall measurement at various temperatures as a function of V_{bg} for 6L MoS_2. The charge carrier concentration linearly increases as a function of back gate voltage.

Layer Number	μ_{imp} (cm^2/Vs)	Carrier Density (cm^{-2})	γ_{ph}
1L (CVD)	1,020	1.1x10^{13}	1.9
2L	3,350	6.9x10^{12}	2.5
3L	1,530	9.3x10^{12}	2.0
4L	7,300	6.9x10^{12}	2.2
6L	34,000	6.8x10^{12}	2.3
1L (Ref.S7)	264	1.9x10^{13}	1.7
2L (Ref.S7)	394	1.3x10^{13}	1.1
4L (Ref.S8)	314	1.2x10^{13}	1.5

Supplementary Table 1 | Comparison and fitting parameters for hBN-encapsulated MoS_2 devices[7,8]**.**

S5. Optical phonon-limited mobility in MoS_2

To attain γ values of hBN-encapsulated MoS_2 devices, we fitted the Hall mobility with temperature as shown in Fig. S7. We assumed Coulomb impurity scattering and phonon scattering as the dominant scattering mechanisms in our work. By applying Matthiessen's rule, total mobility can be expressed with $\frac{1}{\mu(T)} = \frac{1}{\mu_{imp}} + \frac{1}{\mu_{ph}(T)}$, where μ_{imp} is the Coulomb impurity limited mobility at low temperature and μ_{ph} is the one affected by optical phonon of MoS_2 dominant above 100 K[9]. From the Matthiessen's rule, optical phonon-limited mobility (Fig. S7) was extracted by subtracting impurity-limited mobility from the measured Hall mobility and could be well fitted by a power law, $\mu_{ph} \sim T^{-\gamma}$, indicating that optical phonon scattering is dominant above 100 K. We obtained the relatively large γ values of 1.9 - 2.5 among our samples, which shows much stronger temperature-dependence of our hBN-encapsulated MoS_2 devices compared to previously reported values of 0.7 - 1.7 in SiO_2-supported MoS_2 devices.

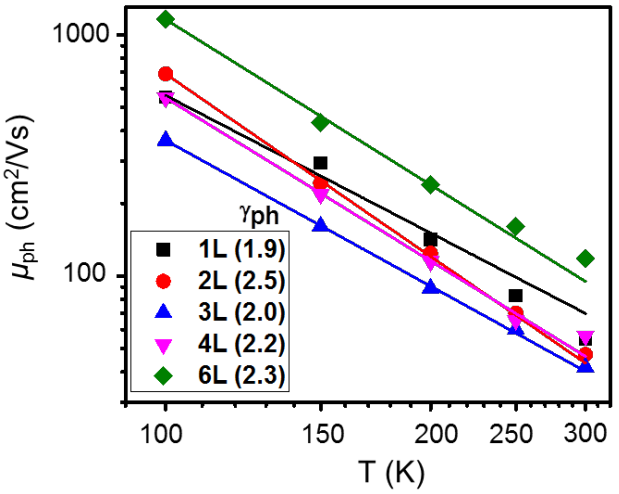

Supplementary Fig. 7 | Optical phonon-limited mobility of MoS_2. The phonon-limited mobilities (μ_{ph}) of hBN-encapsulated MoS_2 devices with different MoS_2 thickness are plotted in the temperature range of 100 - 300 K. By fitting with above 100 K, the values of γ were obtained as shown in the inset of Fig. 3a.

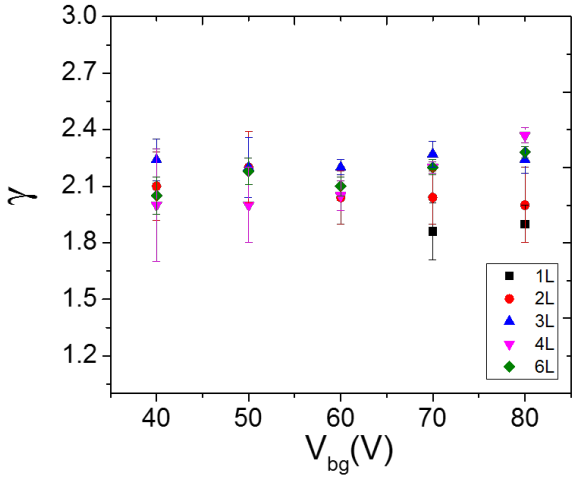

Supplementary Fig. 8 | γ as function of gate voltages. Estimated values of γ as function of gate voltage (charge carrier density) from different MoS_2 thickness are within the experimental uncertainty. It suggests that electron-optical phonon coupling in MoS_2 is not dynamically screened by gate voltage. Notice this plot is calculated based on field-effect mobilites.

S6. Quantum scattering time analysis in MoS_2

We calculate the quantum scattering time in MoS_2 from Shubnikov-de Haas (SdH) oscillations. Comparison of the ratio of the transport scattering time to quantum scattering time by number of layer of MoS_2 will provide the deep understanding about scattering sources in MoS_2. First, transport scattering time $\tau_t = m^*\mu/e$ are obtained from Hall mobility of MoS_2. And, to obtain the quantum scattering time, we used the Ando formula, $\frac{\delta\rho_{xx}}{\rho_0} = 4\gamma_{th}\exp\left(-\frac{\pi}{\omega_c\tau_q}\right)$, where $\gamma_{th} = \frac{2\pi^2 k_B T/\hbar\omega_c}{\sinh(2\pi^2 k_B T/\hbar\omega_c)}$ is Dingle term, ω_c is the cyclotron frequency and τ_q is the quantum scattering time. We also calculate the quantum scattering time from quantum mobility, which are estimated from the onset of SdH oscillation magnetic field. We note that band structure calculations of MoS_2 predict that there are two bands (at the K and Λ points) near the Fermi level, and that for 1L to 3L, the K band ($m^* \sim 0.5m_0$) is lowest in energy, meanwhile the Λ band ($m^* \sim 0.6m_0$) is lowest for > 4L[10]. Figure S9d exhibits the τ_t/τ_q ratio increase as increase of number of layer, and it is due to the long-range scattering origins ($\tau_t/\tau_q > 1$) such as charged impurities and adsorbents become the dominant source of scattering in few-layer MoS_2 which lead dominant small angle scattering that destroy cyclotron orbit motions, while the short-range scattering origins ($\tau_t/\tau_q \sim 1$) such as vacancies, ripple and cracks are dominant at the monolayer MoS_2 by the nature of 2D materials.

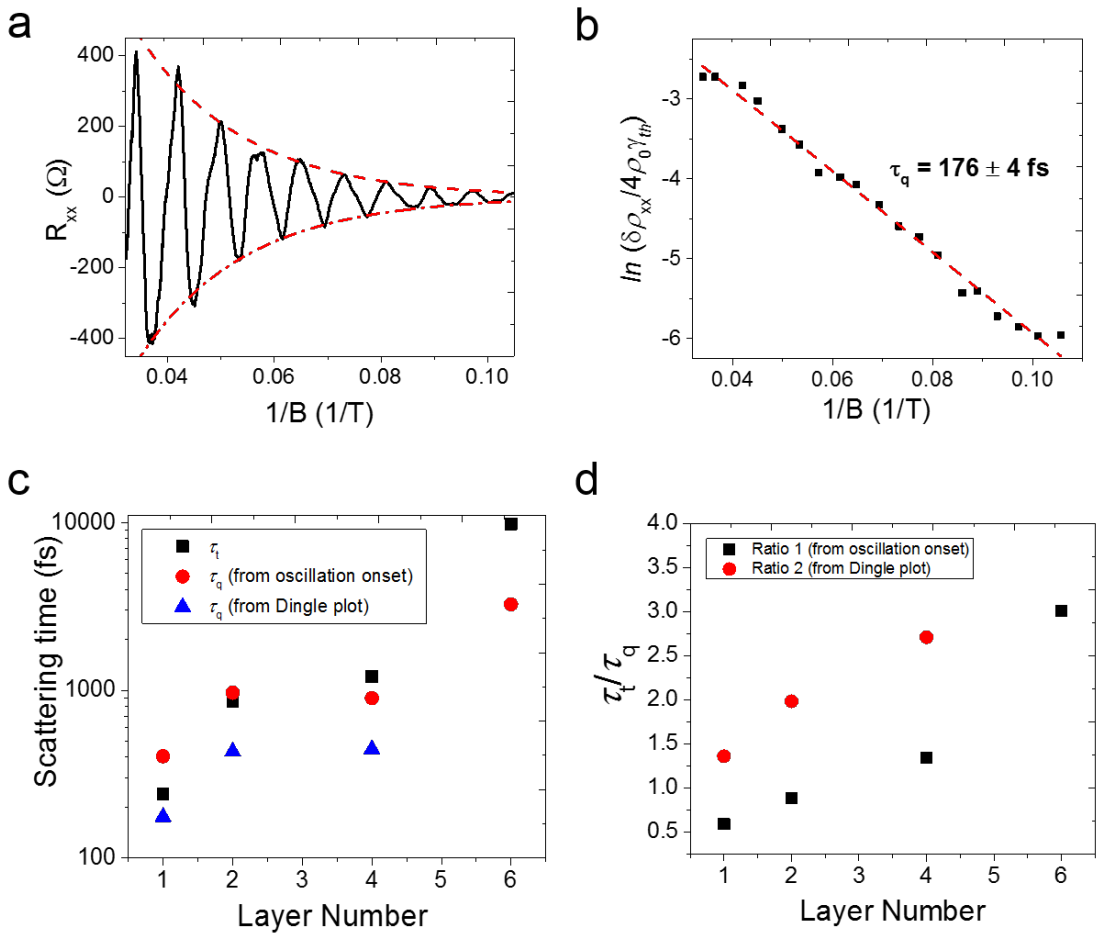

Supplementary Fig. 9 | Quantum scattering time of MoS_2. a, R_{xx} as function of inverse magnetic field of monolayer MoS_2 (solid line) as shown in Fig. 4a and dashed lines correspond to the Ando formula. **b,** Quantum scattering time ($\tau_q = 176 \pm 4$ fs) of monolayer MoS_2 are extracted from the Dingle plot. **c,** Estimated scattering times as function of number of layer of MoS_2. **d,** Ratio of the transport and quantum scattering time (red: from Dingle plot, black: from SdH oscillation onset) as a function of number of layer of MoS_2.

S7. Periodicity analysis of SdH oscillations in monolayer MoS_2

We estimate the charge carrier concentration (n_{SdH}) from the SdH oscillation of monolayer MoS_2 with different gate voltage as shown in Fig. S10a. We analysis the SdH oscillations peaks as function of inverse magnetic field with different gate voltage and we can clearly see the periodicity change as shown in Fig. S10a and S10b. When we compare the total charge carrier concentration (n_t) from the Hall measurements with n_{SdH}, we have to consider the degeneracy of monolayer MoS_2. First, when we assume the spin and valley degeneracy (g = 4) in monolayer MoS_2, n_{SdH} is larger than n_t as shown in Fig. S10c. So degeneracy in monolayer MoS_2 should be smaller than 4, it may be attribute to the strong spin-orbit coupling induced lift of the spin degeneracy ($\Delta E = 1 \sim 10$ meV) at conduction band of monolayer MoS_2. So we need further study about the lift of spin or valley degeneracy of MoS_2 by strong spin-orbit coupling and Zeeman effect under high magnetic field.

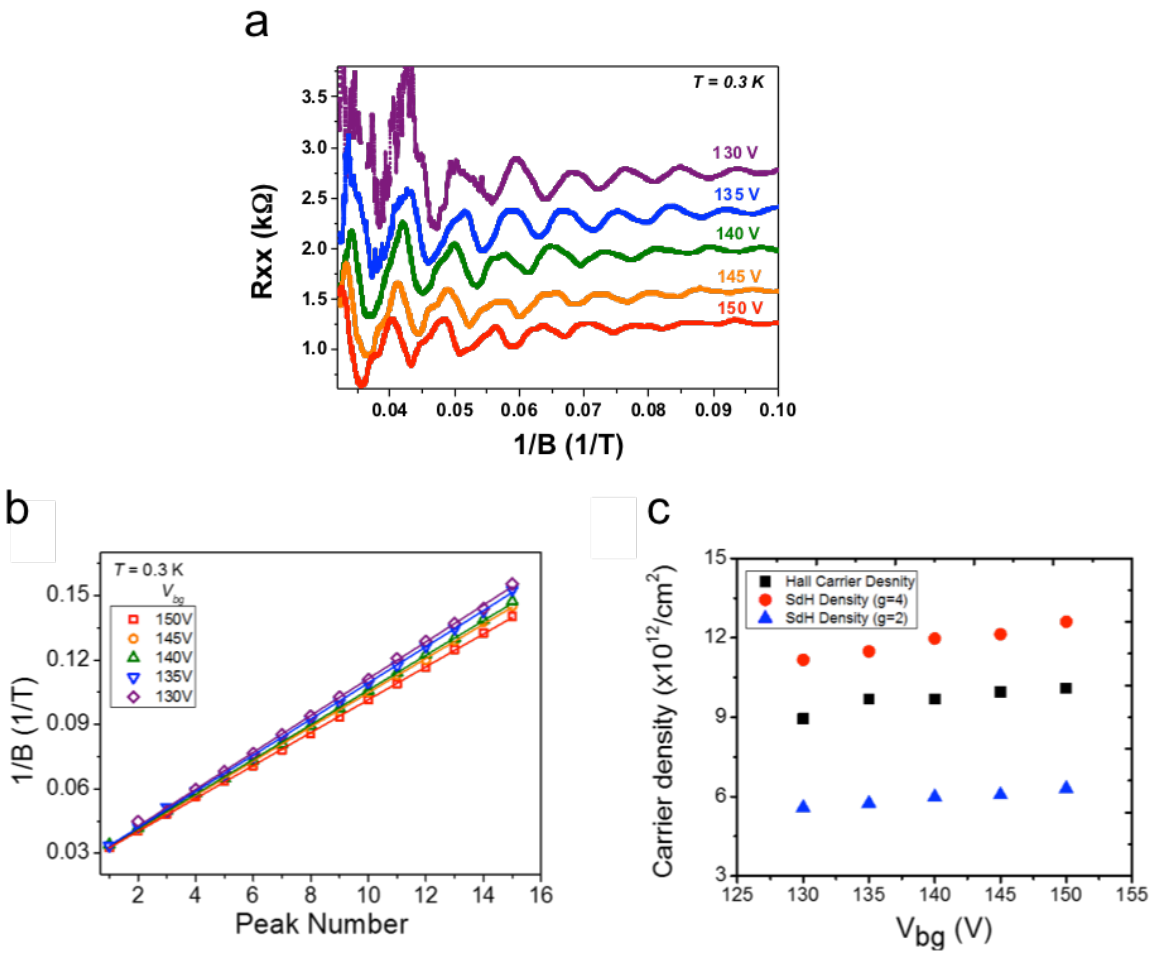

Supplementary Fig. 10 | Periodicity analysis of monolayer MoS_2. a, R_{xx} of monolayer MoS_2 as a function of inverse magnetic field with varying gate voltage. **b,** SdH oscillations peaks as function of inverse magnetic field with different gate voltage. **c,** Estimated charge carrier concentration from SdH oscillation with different degeneracy (red: g = 4, blue: g = 2) and total charge carrier concentration from Hall measurements (black) of monolayer MoS_2.

S6. Modeling MoS_2 electron mobility limited by interfacial Coulomb impurities

A. Electrostatics

The problem consists of a thin layer of semiconductor of thickness t_s, MoS_2 in this case, sandwiched between two dielectrics layers. Let z denotes the direction normal to these layers, and m_z be the quantization mass of MoS_2. We uses a triangular well approximation as an initial estimate to the electrostatics of MoS_2 in the confinement direction, where F_s is its electric field, where the eigen-solutions are known[8]. The eigen-energies E_j must satisfy,

$$Ai(z_0)Bi(z_1) - Ai(z_1)Bi(z_0) = 0 \tag{1}$$

where Ai and Bi are the Airy functions, and

$$z_0 = -\left(\frac{2m_z}{\hbar^2 e^2 F_s^2}\right)^{1/3} E_j \ \ , \ \ z_1 = \left(\frac{2m_z e F_s}{\hbar^2}\right)^{1/3}\left(t_s - \frac{E_j}{eF_s}\right)$$

The eigen-functions are then given by,

$$\psi_j(z) = aAi\left[\left(\frac{\pi}{v}\right)^{2/3}\left(\frac{vz}{t_s} - \gamma\right)\right] + bBi\left[\left(\frac{\pi}{v}\right)^{2/3}\left(\frac{vz}{t_s} - \gamma\right)\right] \tag{2}$$

where $v = eF_s t_s/\eta$, $\eta = \hbar^2\pi^2/2m_z t_s^2$ and $\gamma = E_j/\eta$. Within this triangular model approximation, the electric fields in the different regions are related via $\epsilon_{ox1}F_{ox1} = \epsilon_s F_s = \epsilon_{ox2}F_{ox2}$. The carrier densities can be computed from,

$$\begin{aligned} n &= \sum_{i,v} \frac{g_v m_d^v}{\pi\hbar^2} \int_{E_{i,v}}^{\infty} \frac{1}{\exp\left(\frac{E-E_f}{kT}\right)+1} dE\, |\psi_{i,v}(z)|^2 \\ &= \frac{kT}{\pi\hbar^2} \sum_{i,v} g_v m_d^v \ln\left[\exp\left(\frac{E_f - E_{i,v}}{kT}\right)+1\right] |\psi_{i,v}(z)|^2 \end{aligned} \tag{3}$$

where i and v denotes the subbands and valleys. g_v is the valley degeneracy. m_d is the density of states mass. The Fermi energy E_f is determined from Eq. 3, by imposing that $n = C_{ox}V_g$.

The solutions to the triangular well approximation provides an initial guess to the electrostatics. With this, we solved the multilayers MoS_2 electrostatics by solving the Poisson and Schrödinger equation self-consistently within the effective mass framework. In this work, we include both the K and Λ valleys, with band edge energies that are close to one another in multilayers MoS_2. With reference to calculations obtained from density

functional theory[11–14], we extract the in-plane and out-of-plane masses: $m_{d,K} = 0.5m_0$, $m_{d,\Lambda} = 0.6m_0$, $m_{z,K} = 1.5m_0$, $m_{z,K} = 1.0m_0$. Due to their different m_z, the two valleys have different band edge energy offset depending on the MoS_2 thickness, and is taken to be zero when $t_s = 4\,\text{nm}$. Their valley degeneracies are $g_{v,K} = 2$ and $g_{v,\Lambda} = 6$.

B. Screened Interfacial Coulomb potential

To calculate the scattering rate due to Coulomb centers, we must first find the scattering potential induced by a point charge. This Coulomb potential is governed by the following Poisson equation;

$$\nabla\epsilon(\vec{r},z)\nabla\phi(\vec{r},z,z_0) = -e\delta(z-z_0) - e\rho_{ind} \tag{4}$$

where $\vec{r}$ is the $2D$ position vector describing the plane perpendicular to the gate confinement direction. The presence of the external point charge resulted in a Coulomb potential $\phi(\vec{r},z,z_0)$ which also induced charge ρ_{ind}. Next, we need to obtain an expression for ρ_{ind}.

Here, we employed a perturbative approach by Stern[9] commonly used in the context of semiconductor devices. The presence of the perturbation potential $\phi(z)$ results in correction of the eigen-energies $\delta E_{i,v} = -e\int \phi(z)\left|\psi_{i,v}(z)\right|^2 dz$. The charge induced ρ_{ind} is the change in the amount of charge due to the change in eigen-energies $\delta E_{i,v}$;

$$\begin{aligned}
\rho_{ind}(z) &= -e\sum_{i,v}\frac{dn_{i,v}}{dE_{i,v}}\delta E_{i,v} \\
&= -\sum_{i,v}\frac{g_v m_d^v e^2}{\pi\hbar^2}\frac{1}{1+\exp\left(\frac{E_{i,v}-E_f}{kT}\right)}\left|\psi_{i,v}(z)\right|^2\int\phi(z')\left|\psi_{i,v}(z')\right|^2 dz' \qquad (5)\\
&\equiv -\sum_{i,v}S_{i,v}\left|\psi_{i,v}(z)\right|^2\int\phi(z')\left|\psi_{i,v}(z')\right|^2 dz' \qquad (6)
\end{aligned}$$

Hence, Eq.4 can be approximated by the following;

$$\nabla\epsilon(\vec{r},z)\nabla\phi(\vec{r},z,z_0) = -e\delta(z-z_0) + e\sum_{i,v}S_{i,v}\left|\psi_{i,v}(z)\right|^2\int\phi(\vec{r},z')\left|\psi_{i,v}(z')\right|^2 dz'$$

This is the key result by Stern[9].

It renders the problem easier to express the in-plane part of thr potential $\phi(\vec{r},z,z_0)$ in its $2D$ Fourier representation,

$$\phi(\vec{r},z,z_0) = \sum_{\vec{q}}\tilde{\phi}_{\vec{q}}\exp(i\vec{q}\cdot\vec{r})\phi_0(z,z_0)$$

Thus we have the Poisson equation in the semiconductor region;

$$\epsilon_{sc}\nabla^2\phi_0(z,z_0) - \epsilon_{sc}q^2\phi_0(z,z_0) = -e\delta(z-z_0) + e\underbrace{\sum_{i,v} S_{i,v}\left|\psi_{i,v}(z)\right|^2 \int \phi_0(z',z_0)\left|\psi_{i,v}(z')\right|^2 dz'}_{K(z_1,z_0)} \quad (7)$$

Here, $\epsilon_{sc} = 7.4$ is the out-of-plane dielectric constant of MoS_2 [10]. Multiply by $1/q\cdot\exp(-q|z-z_1|)$ with $0 < z < t_s$ and integrating for $0 < z_1 < t_s$, we arrived at,

$$\phi_0(z,z_0) = -\frac{e}{2q\epsilon_{sc}}\int_0^{t_s}\exp\left(-q|z-z_1|\right)K(z_1,z_0)dz_1 + \frac{e}{2q\epsilon_{sc}}\int_0^{t_s}\exp\left(-q|z-z_1|\right)\delta(z_1-z_0)dz_1 \quad (8)$$

Note we assume the semiconductor is sandwiched by dielectrics, i.e. no metal gates. Otherwise, we have additional terms given by $A(q)\exp(-qz) + B(q)\exp(qz)$ to account for screening by the metals.

C. Mobility

With $\phi_0(\vec{q},z,0)$, one uses Fermi Golden rule to obtain the scattering probability;

$$P(\vec{k}_i,\vec{k}_j) = N_{im}\frac{2\pi}{\hbar}\left|e\int_0^{\infty}\phi_0(\vec{q},z,0)\psi_i(z)\psi_j(z)dz\right|^2\delta\left(E(\vec{k}_i) - E(\vec{k}_j)\right) \quad (9)$$

where $k_i = \sqrt{2m_d^i/\hbar^2(E-E_i)}$, $\vec{q} = \vec{k_j} - \vec{k_i}$ and θ is the angle between the initial and final wave vector. N_{im} is the impurities concentration. To calculate the relaxation time, we write,

$$\begin{aligned}
\frac{1}{\tau_i(\vec{k}_i)} &= \sum_{\vec{k}'_j} P(\vec{k}_i,\vec{k}'_j)\left[1 - \frac{\tau_j(\vec{k}'_j)k'_j m_{c,j}}{\tau_i(\vec{k}_i)k_i m_{c,i}}\cos(\theta)\right]\delta\left(E(\vec{k}_i) - E(\vec{k}_j)\right) \\
\frac{1}{\tau_i(E_i)} &= \frac{m_{d,i}}{\pi\hbar^3}\sum_j\int_0^{\pi}\left|e\int_0^{\infty}\phi_0(\vec{q},z,0)\psi_i(z)\psi_j(z)dz\right|^2\delta\left(E_i - E_j\right)\left[1 - \frac{\tau_j(E_i)k'_j m_{c,j}}{\tau_i(E_i)k_i m_{c,i}}\cos(\theta)\right]d\theta \\
\Rightarrow \frac{1}{\tau_i(E)} &\equiv \sum_j\left\{A_{i,j} - B_{i,j}\frac{\tau_j(E)}{\tau_i(E)}\right\} \quad (10)
\end{aligned}$$

where m_c is the transport mass. The above can be re-expressed into an equivalent matrix form as follows;

$$\begin{pmatrix} 1 \\ 1 \\ 1 \\ 1 \\ \vdots \end{pmatrix} = \begin{pmatrix} \sum_j A_{1j} & -B_{12} & -B_{13} & -B_{14} & \cdots \\ -B_{21} & \sum_j A_{2j} & -B_{23} & -B_{24} & \cdots \\ -B_{31} & -B_{32} & \sum_j A_{3j} & -B_{34} & \cdots \\ -B_{41} & -B_{42} & -B_{43} & \sum_j A_{4j} & \cdots \\ \vdots & \vdots & \vdots & \vdots & \ddots \end{pmatrix}\begin{pmatrix} \tau_1(E) \\ \tau_2(E) \\ \tau_3(E) \\ \tau_4(E) \\ \vdots \end{pmatrix} \quad (11)$$

which can easily be solved by inverting the matrix above. The relaxation time can be similarly computed for the other valley.

The mobility for each subband j and valley v then follows from,

$$\mu_{jv} = -\frac{e}{m_{c,v}} \frac{\int (E - E_f)\tau_{jv}(E) \frac{\partial f(E,E_f)}{\partial E} dE}{\int f(E, E_f) dE} \tag{12}$$

where $f(E, E_f)$ is the Fermi-Dirac distribution function. The total effective mobility is then

$$\mu_{eff} = \frac{\sum n_{j,v}\mu_{j,v}}{\sum n_{j,v}} \tag{13}$$

where $n_{j,v}$ is the carrier densities in subband j and valley v.

D. Short-range scattering potential

In the main manuscript, we discussed two tpyes of short-range scattering potential i.e. bulk and interfacial. The former could be due to atomic defects such as S vacancies in MoS_2 itself, which is present in its natural crystal form. The latter, interfacial short-range scatterers, could be due to presence of chemical adsorbates that was introduced to the top interface due to subsequent processing steps after MoS_2 transfer onto the SiO_2 substrate. As explained in the main manuscript, we found the latter model to agree better to the experiments. We model the short-range scatterers at the top MoS_2 interface (i.e. $z = 0$) within the same framework describe above by simply making the replacement to the scattering potential in Eq. 9 i.e. $\phi_0(\vec{q}, z, 0) \rightarrow v_{sc}\delta(z)$ and N_{sc} denotes the short-range scatterers concentration (cm^{-2}). On the other hand, the scattering potentials are distributed across the different layers of MoS_2 when modeling of bulk short-range scatterings. In the case of S vacancies in MoS_2, the total short-range scatterers concentration (cm^{-2}) increases with layer thickness and one expects a decrease in electron mobility with layer thickness contrary to what is observed in our experiments. We therefore focus only on interfacial short-range scattering potential in this work.

E. Calculation results

Here we show results of our calculation for both interfacial Coulomb impurities and short-range scatterers located at the top MoS_2 interface. The long-range Coulomb limited moblity, μ_{LR}, predicts a layer dependence weaker than the experiments of less than an order of magnitude within the range of carrier densities considered, while the short-range limited mobility, μ_{SR}, predicts a much stronger thickness dependence larger than 4 orders of magnitude. In sum, their total contribution according to Matthiessen rule would allow for better quantitative agreement with the experiments.

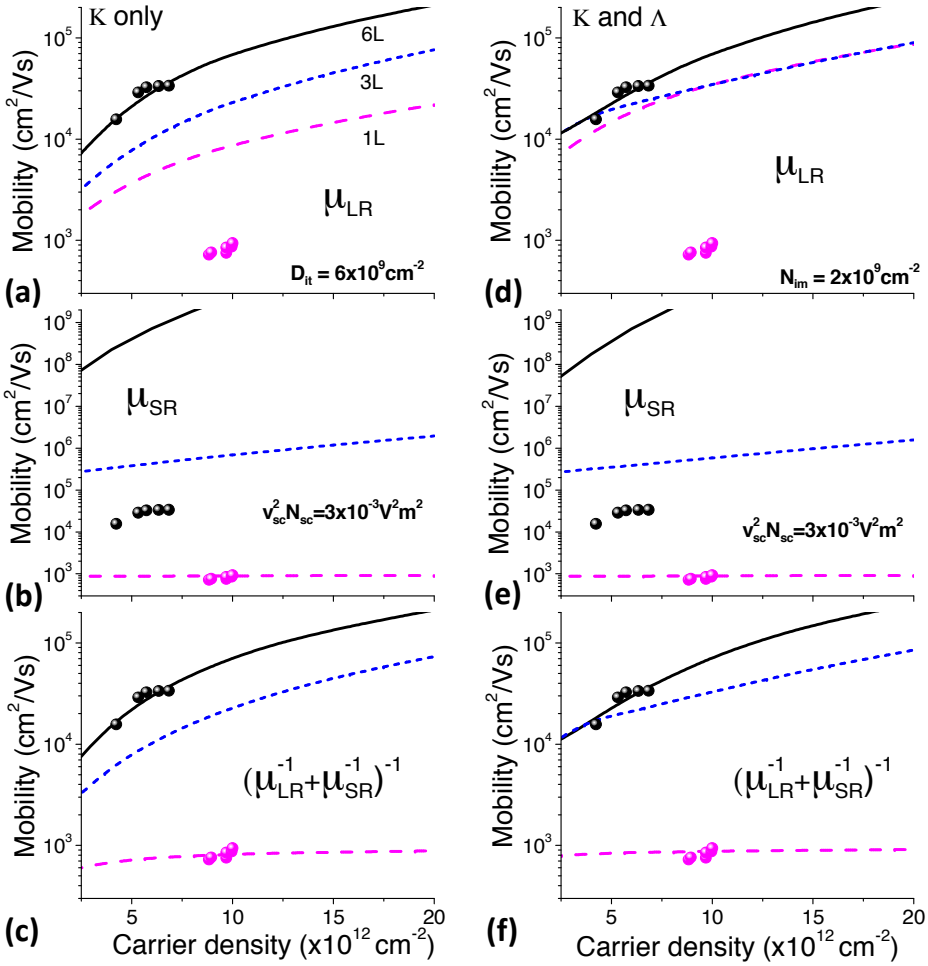

Fig. S8: Calculated electron mobility due to interfacial Coulomb impurities (μ_{LR}) and short-range scatterers (μ_{SR}) located at the top MoS_2 interface as function of gate bias and for different number of MoS_2 layers. We consider two cases, one where only K valleys are considered in (a-c), and where both K and Λ valleys are included in (d-f). We also displayed the experimentally measured low temperature mobilities for 1L and 6L devices. We found that the calculated μ_{LR} predicts a layer dependence weaker than the experiments, while the calculated μ_{SR} predicts a much larger thickness dependence. In sum, their total contribution according to Matthiessen rule would allow for better quantitative agreement with the experiments.

References

S1. Lee, GH. *et al.* Flexible and transparent MoS_2 field-effect transistors on hexagonal boron nitride-graphene heterostructures. *ACS Nano* **7**, 7931-7936 (2013).

S2. Wang, L. *et al.* One-Dimensional Electrical Contact to a Two-Dimensional Material. *Science* **342**, 614–617 (2013).

S3. Mak, K., Lee, C., Hone, J., Shan, J. & Heinz, T. Atomically Thin MoS_2: A New Direct-Gap Semiconductor. *Phys. Rev. Lett.* **105**, 136805 (2010).

S4. Lee, C. *et al.* Anomalous lattice vibrations of single-and few-layer MoS_2. *ACS Nano* **4**, 2695-2700 (2010).

S5. Yu, L. *et al.* Graphene/MoS_2 Hybrid Technology for Large-Scale Two-Dimensional Electronics. *Nano Lett.* **14**, 3055-3063 (2014).

S6. Roy, T. *et al.* Field-Effect Transistors Built from All Two-Dimensional Material Components. *ACS Nano* **8**, 6256-6264 (2014).

S7. Baugher, B., Churchill, H., Yang, Y. & Jarillo-Herrero, P. Intrinsic Electronic Transport Properties of High-Quality Monolayer and Bilayer MoS_2. *Nano Lett.* **13**, 4212–4216 (2013).

S8. Neal, A., Liu, H., Gu, J. & Ye, P. Magneto-transport in MoS_2: phase coherence, spin-orbit scattering, and the hall factor. *ACS Nano* **7**, 7077–1082 (2013).

S9. Ma, N. & Jena, D. Charge Scattering and Mobility in Atomically Thin Semiconductors. *Phys. Rev. X* **4**, 011043 (2014).

S10. Liu, G.-B., Shan, W.-Y., Yao, Y., Yao, W. & Xiao, D. Three-band tight-binding model for monolayers of group-VIB transition metal dichalcogenides. *Phys. Rev. B* **88,** 085433 (2013).

S11. Miller, David AB. "Quantum mechanics for scientists and engineers." Cambridge University Press, Cambridge (2008)

S12. Stern, Frank, and W. E. Howard. "Properties of semiconductor surface inversion layers in the electric quantum limit." *Phys. Rev.* **163**, 816 (1967)

S13. Molina-Sanchez, Alejandro, and Ludger Wirtz. "Phonons in single-layer and few-layer MoS_2 and WS_2." *Phys. Rev. B* **84**, 155413 (2011)

S14. Han, S. W., Hyuksang Kwon, et al. "Band-gap transition induced by interlayer van der Waals interaction in MoS_2." *Phys. Rev. B* **84**, 045409 (2011)

S15. Zhao, Weijie, Ricardo Mendes Ribeiro, et al. "Origin of Indirect Optical Transitions in Few-Layer MoS_2, WS_2, and WSe_2." *Nano Lett.* **13**, 5627-5634 (2013)

S16. Wickramaratne, Darshana, Ferdows Zahid, and Roger K. Lake. "Electronic and thermoelectric properties of few-layer transition metal dichalcogenides." *J. Chem. Phys.* **140**, 124710 (2014)

S17. Cheiwchanchamnangij, Tawinan, and Walter RL Lambrecht. "Quasiparticle band structure calculation of monolayer, bilayer, and bulk MoS_2." *Phys. Rev. B* **85**, 205302 (2012)